

# 1 Quantifying uncertainty in brain-predicted age using scalar-on-image 2 quantile regression

3 Marco Palma<sup>a,\*</sup>, Shahin Tavakoli<sup>a</sup>, Julia Brettschneider<sup>a,b</sup>, Thomas E. Nichols<sup>a,c,d</sup>, for the  
4 Alzheimer's Disease Neuroimaging Initiative<sup>1</sup>

5 <sup>a</sup>*Department of Statistics, University of Warwick, Coventry, CV4 7AL, United Kingdom*

6 <sup>b</sup>*The Alan Turing Institute, London, NW1 2DB, United Kingdom*

7 <sup>c</sup>*Oxford Big Data Institute, Li Ka Shing Centre for Health Information and Discovery, Nuffield Department of  
8 Population Health, University of Oxford, Oxford, OX3 7LF, United Kingdom*

9 <sup>d</sup>*Wellcome Centre for Integrative Neuroimaging, FMRIB, Nuffield Department of Clinical Neurosciences,  
10 University of Oxford, Oxford, OX3 9DU, United Kingdom*

---

## 11 Abstract

12 Prediction of subject age from brain anatomical MRI has the potential to provide a sensitive  
13 summary of brain changes, indicative of different neurodegenerative diseases. However, existing  
14 studies typically neglect the uncertainty of these predictions. In this work we take into account  
15 this uncertainty by applying methods of functional data analysis. We propose a penalised func-  
16 tional quantile regression model of age on brain structure with cognitively normal (CN) subjects  
17 in the Alzheimer's Disease Neuroimaging Initiative (ADNI), and use it to predict brain age in Mild  
18 Cognitive Impairment (MCI) and Alzheimer's Disease (AD) subjects. Unlike the machine learning  
19 approaches available in the literature of brain age prediction, which provide only point predictions,  
20 the outcome of our model is a prediction interval for each subject.

21 *Keywords:* brain age, scalar-on-image regression, prediction intervals, quantile regression.

---

## 22 1. Introduction

23 The process of brain ageing is known to be associated to a general decline in cognitive functions  
24 and higher risk of neurodegenerative diseases (Yankner et al., 2008; Denver and McClean, 2018).  
25 In some cases, both ageing and dementia affect the same areas in the brain (Lockhart and DeCarli,  
26 2014). For these reasons, a deeper understanding of brain ageing in healthy conditions could  
27 potentially improve the diagnosis of neurodegeneration at early stages.

28 Neuroimaging provides a non-invasive and safe way to study brain structure and functioning. A  
29 large part of the research in neuroimaging data analysis has been focused on explanatory analyses

---

\*Corresponding author

*Email address:* M.Palma@warwick.ac.uk (Marco Palma)

<sup>1</sup>Data used in this work were obtained from the Alzheimer's Disease Neuroimaging Initiative (ADNI) database (<http://adni.loni.usc.edu>). As such, the investigators within the ADNI contributed to the design and implementation of ADNI and/or provided data but did not participate in analysis or writing of this work. A complete listing of ADNI investigators can be found at: [http://adni.loni.usc.edu/wp-content/uploads/how\\_to\\_apply/ADNI\\_Acknowledgement\\_List.pdf](http://adni.loni.usc.edu/wp-content/uploads/how_to_apply/ADNI_Acknowledgement_List.pdf).

30 aimed at describing the relationship between the brain and some variables of interest (such as  
31 neurodegenerative diseases, sex, physical activity). With the advent of large imaging databases, a  
32 prediction-oriented focus has been also considered, in order to detect individual differences among  
33 subjects that could be used in clinical practice (for example [Yoo et al., 2018](#); [Zhou et al., 2019](#)).

34 The study of brain ageing has recently gained attention in the neuroscientific community thanks  
35 to the availability of this large amount of data and of computational tools for their analysis. A  
36 growing body of research employs neuroimaging to develop a biomarker of individual brain health,  
37 called “brain age” ([Franke and Gaser, 2019](#); [Cole et al., 2017](#)). In the absence of a clear definition  
38 and assessment of biological brain age, a brain-derived prediction of chronological age is considered.  
39 In order to be integrated in clinical practice, a brain age biomarker should be easily accessible from  
40 brain data (or better, images), harmless for the subjects, computationally not demanding and  
41 correlated with other brain health indicators ([Franke and Gaser, 2019](#)). In addition, since there is  
42 a high variability between subjects in terms of their brain ageing, a useful biomarker should predict  
43 cognitive decline better than the chronological age itself.

44 In this work we propose a statistically grounded workflow that produces brain age individual  
45 predictions from 3-dimensional brain images. Furthermore, we go beyond simple point predictions  
46 by also providing prediction intervals of the brain age to quantify the uncertainty. Our model is  
47 trained on a control group with no ongoing brain diseases in order to avoid spurious effects due  
48 to other conditions. The same model can be used to predict age in neurodegenerative diseases,  
49 in order to provide a “baseline” or “normative” brain age, whose difference from the individual  
50 chronological age (brain-predicted age difference or *brainPAD* as in [Cole et al., 2017](#)) might inform  
51 about the extent of the effect induced by the pathology.

52 In addition, the prediction interval approach offers another potential binary biomarker (whether  
53 the chronological age falls within it). Since the width of the prediction interval is different for each  
54 subject, the same brainPAD could be interpreted in different ways in light of its location with  
55 respect to the individual prediction limits. The joint use of point and interval brain age predictions  
56 could therefore be employed to easily assess departures from a typical ageing profile.

57 The approach developed in this paper is based on modern statistical tools. In order to use 3D  
58 brain images without the need to summarise information by regions of interest, a functional data  
59 analysis (FDA) framework is adopted ([Ramsay and Silverman, 2005](#); [Horváth and Kokoszka, 2012](#)).

60 Functional data get this name because the observation for each statistical unit is a function<sup>2</sup> (a  
61 curve, surface, or image). These data are usually considered as infinite dimensional and intrinsically  
62 continuous, even if the data collection process reduces them to a discrete series of observed points  
63 (Ramsay and Silverman, 2005, Section 3.2). In other words, the whole function is considered as the  
64 object of interest, and not only the specific value observed at a discrete location for each image.  
65 A common model in FDA is scalar-on-function regression (see Morris, 2015; Reiss et al., 2017 for  
66 reviews), which provides an effective way to predict a scalar quantity of interest from a functional  
67 observation, by fitting a regression model using the whole function as a covariate. In our context we  
68 call it *scalar-on-image regression*. The non-identifiability problem (Happ et al., 2018) arising from  
69 having sample size lower than the number of voxels for each image can be attenuated by imposing  
70 some assumptions on the data generating process (for example smoothness).

71 We obtain prediction intervals by integrating the FDA framework with quantile regression  
72 (Koenker and Bassett, 1978; Koenker and Hallock, 2001), a model that is largely used in fields  
73 such as economics (Fitzenberger et al., 2013) and ecology (Cade and Noon, 2003) to derive a more  
74 complete picture of the relationship between a covariate and the response variable. Quantile re-  
75 gression does not model the expected value (or a function of it) of the outcome of interest given the  
76 predictors, but some selected quantiles of the conditional distribution (for example the median).  
77 This model can be adapted for functional covariates: in a functional quantile regression model we  
78 explore the linear relationship between a certain quantile of the outcome and the 3D image. By  
79 fitting several quantile regression models we can build the prediction intervals given the covariates.  
80 Prediction intervals from quantile regression (or similar models) have received some attention in  
81 recent decades (Zhou and Portnoy, 1996; Meinshausen, 2006; Mayr et al., 2012), but not within  
82 the framework of functional data. In addition, the scalar-on-image quantile regression generates a  
83 regression coefficient with the same dimensionality as the brain image, providing an interpretable  
84 map that shows how the changes in each brain structure are related to the predicted age.

85 Our FDA-based approach departs considerably from other methods that are commonly used in  
86 the neuroimaging literature. The current state-of-the-art method in neuroimaging data analysis is  
87 the so-called *mass-univariate* approach implemented in the *Statistical Parametric Mapping* software  
88 (Ashburner et al., 2014). A model is fitted to predict the signal at each voxel independently using

---

<sup>2</sup>the word “functional” in this case is used in a mathematical sense and is not related to functional MRI.

89 the clinical or demographic information as covariate, then a significance map is produced (see for  
90 further details [Friston et al., 1994](#); [Penny et al., 2011](#)). Although computationally efficient, this  
91 approach does not explicitly model the spatial correlation of adjacent pixels and is not tailored  
92 for prediction purposes ([Reiss and Ogden, 2010](#)). The functional data approach allows instead the  
93 incorporation of the spatial structure by using smoothing techniques and in this way the fit of a  
94 global model for a scalar outcome given the entire brain image.

95 Another popular approach is based on machine learning algorithms. [Franke and Gaser \(2019\)](#)  
96 review a collection of studies published in the last decade based on a technique called relevance  
97 vector regression. They review a number of studies that examine associations with brain age,  
98 including effects of meditation and playing an instrument. [Cole et al. \(2019\)](#) collects a larger  
99 number of studies dealing with brain age prediction conducted from 2007 to 2018 with different  
100 imaging modalities and pathologies. Many of them adopt support vector regression (as the ones  
101 listed in [Franke et al., 2012](#); [Franke and Gaser, 2019](#) or [Sone et al., 2019](#)) or more recently Gaussian  
102 processes and convolutional neural networks ([Cole et al., 2017](#); [Cole, 2017](#); [Varatharajah et al., 2018](#);  
103 [Wang et al., 2019](#)). A comparison between the predictive performances of these methods is difficult  
104 due to the use of different datasets and different age ranges, but according to [Cole et al. \(2019\)](#)  
105 the choice of the algorithm does not seem to play a fundamental role. However, these approaches  
106 provide only a point prediction with little knowledge of the internal procedure that returned it, and  
107 in particular deep learning methods are often criticised as “black boxes”. Our approach attempts  
108 to provide a better picture of the set of information on which brain age is based, introducing a  
109 straightforward quantification of uncertainty and at the same time producing a visual display of  
110 the regions that are most relevant for the prediction. In addition, the features of each step of the  
111 workflow proposed here can be evaluated, therefore improving the interpretability of the results.  
112 This last aspect is crucial in medical sciences and is particularly welcome for predictive modelling  
113 in neuroscience ([Scheinost et al., 2019](#)).

114 Another important distinction with the available literature on brain age prediction relates to the  
115 imaging techniques used. Although several models use functional imaging or multiple modalities,  
116 a large share of studies focused on structural magnetic resonance imaging (MRI), in particular T1-  
117 weighted images, usually segmented into grey and white matter. Unprocessed MR images have  
118 also been employed with success ([Cole et al., 2017](#)). In this work we still remain in the family of  
119 structural imaging but we use tensor-based morphometry (TBM) images, that are obtained after

120 a transformation of standard MRI images. TBM images give information about relative volumes  
121 of brain structures with respect to a common template; for this reason the images are all spatially  
122 registered. TBM quantifies volumetric differences in brain tissue for each voxel and is therefore  
123 specifically aimed at assessing the level of local cortical atrophy which might help to study brain  
124 degeneration for different diseases (Hua et al., 2008). To the best of our knowledge, this is the  
125 first study addressing brain age prediction from TBM images. The dataset used in this manuscript  
126 comes from the Alzheimer’s Disease Neuroimaging Initiative (ADNI, Mueller et al., 2005).

127 The work is structured as follows. Section 2 gives an overview of functional data analysis and  
128 quantile regression. Section 2.4 introduces the plan of the analysis and discusses details of the  
129 implementation. The main characteristics of the ADNI dataset are described in Section 3, while  
130 the results of the analysis are reported in Section 4 in terms of the predictions, their robustness  
131 with respect to the choices of the parameters in the model and their correlation with standard  
132 cognitive measures. Finally, Section 5 discusses the main findings, summarises the work and briefly  
133 introduces further research directions.

## 134 2. Materials and Methods

### 135 2.1. Functional data analysis

136 Functional data are realisations of a random function  $X \in L^2(T)$ , the space of square-integrable  
137 functions  $f : T \rightarrow \mathbb{R}$ , for which

$$138 \int_T [f(t)]^2 dt < \infty. \quad (1)$$

139 Typically in FDA we assume  $T \subseteq \mathbb{R}^d$  (Kokoszka and Reimherr, 2017; Ramsay and Silverman, 2005;  
140 Ferraty and Vieu, 2006). We define the inner product

$$141 \langle f, g \rangle = \int_T f(t)g(t)dt, \quad (2)$$

142 and the norm

$$143 \|f\|_{L^2} = \left( \int_T [f(t)]^2 dt \right)^{\frac{1}{2}}, \quad (3)$$

144 where  $f, g \in L^2(T)$ . The first order moment of  $X$  is the mean function  $\mu(t) = \mathbb{E}[X(t)]$ ; the second  
145 order variations of  $X$  are encoded in the covariance function

$$146 v(s, t) = \mathbb{E}[(X(s) - \mu(s))(X(t) - \mu(t))], \quad s, t \in T \quad (4)$$

147 of which the variance function is a special case ( $s = t$ ). A central object when dealing with functional  
148 data is the covariance operator, whose kernel is the covariance function  $v(s, t)$ . It is defined as

$$149 \quad \Gamma(f) = \mathbb{E}[\langle X - \mu, f \rangle (X - \mu)], \quad \forall f \in L^2(T). \quad (5)$$

150 The covariance operator transforms a function  $f$  in another function  $\Gamma(f)$  whose values are

$$151 \quad \Gamma(f)(t) = \int_T v(t, s) f(s) ds, \quad \forall t \in T. \quad (6)$$

152 The covariance operator plays a key role in the Karhunen–Loève expansion for square-integrable  
153 functions,

$$154 \quad X(t) = \mu(t) + \sum_{m=1}^{\infty} \nu_m \psi_m(t), \quad (7)$$

155 expressing  $X$  as an infinite linear combination of the deterministic eigenfunctions  $\{\psi_m(t)\}$  of  $\Gamma$  with  
156 random and uncorrelated weights  $\nu_m$ . The eigenfunctions are the solutions of the eigendecomposi-  
157 tion problem

$$158 \quad \int_T v(t, s) \psi_j(s) ds = \lambda_j \psi_j(t), \quad \forall t \in T. \quad (8)$$

159 The eigenfunctions are orthogonal and rescaled to have unit norm, and their corresponding eigen-  
160 values  $\{\lambda_j\}$  are in decreasing order.

161 The results of the eigendecomposition of the covariance operator can be interpreted under the  
162 framework of functional principal component analysis (FPCA), which aims at studying the principal  
163 modes of variation of the random function  $X$ . The eigenvalue  $\lambda_m$  is the part of the variance of  
164  $X$  explained by the  $m$ -th eigenfunction, also called functional principal component. The random  
165 variables

$$166 \quad \nu_m = \langle X - \mu, \psi_m \rangle \quad (9)$$

167 are called *scores*. The scores are uncorrelated and centered with variance  $\lambda_m$ .

## 168 2.2. Quantile regression

169 Regression models are used to study the relationship between some fixed and known predictors  
170  $Z = (z_1, \dots, z_M)^T \in \mathbb{R}^M$  and an outcome variable  $Y$ . For example, linear models are used to  
171 evaluate the change in the expected value of the continuous outcome conditioned on the values of  
172 the predictors, under specific assumptions on the error term. Nevertheless, there are occasions in  
173 which either these assumptions do not hold (for example, when there is heteroskedasticity in the

residuals) or simply the main interest is to model specific quantiles of the conditional distribution of the response variable in order to produce a deeper analysis of the randomness of  $Y|Z$  that goes beyond the conditional mean<sup>3</sup>. Quantile regression (Koenker and Bassett, 1978) can effectively deal with these cases by specifying the model:

$$Q_\tau(Y|Z) = \alpha_\tau + \sum_{m=1}^M z_m \gamma_{m,\tau}, \quad \tau \in (0, 1), \quad (10)$$

where  $Q_\tau(Y|Z)$  is the  $\tau$ -th conditional quantile of  $Y|Z$  defined as

$$Q_\tau(Y|Z = z) = \inf\{y : F_{Y|Z}(y|z) \geq \tau\} \quad (11)$$

and

$$F_{Y|Z}(y|z) = \Pr(Y \leq y|z) \quad (12)$$

is the conditional cumulative distribution function of  $Y|Z$ . For example,  $Q_{0.5}(Y|Z)$  is the median of the conditional distribution of  $Y|Z$ . The interpretation of  $\gamma_{m,\tau}$  is similar to the one in linear models: it corresponds to the marginal effect on the conditional quantile due to a one-unit increment in the  $m$ -th covariate.

Given  $n$  observations, the estimation procedure for the model in Equation (10) is based on the following minimisation problem:

$$(\hat{\alpha}_\tau, \hat{\gamma}_{1,\tau}, \dots, \hat{\gamma}_{M,\tau}) = \arg \min_{\alpha, \gamma_1, \dots, \gamma_M} \left[ \sum_{i=1}^n \rho_\tau \left( y_i - \alpha - \sum_{m=1}^M z_{im} \gamma_m \right) \right], \quad (13)$$

where  $\rho_\tau(u) = [\tau - \mathbb{1}_{\{u \leq 0\}}] u$  is the check (or quantile loss) function (Koenker and Bassett, 1978). There is a relationship between the linear formulation  $Y = Z\gamma + \varepsilon$  and the quantile formulation in Equation (10). Under a linear data generating process  $Y = \alpha + Z\gamma + \varepsilon$  with known  $\alpha$  and  $\gamma$ , we can write the conditional quantile restriction

$$Q_\tau(Y|Z) = \alpha + Z\gamma + F_\varepsilon^{-1}(\tau), \quad \tau \in (0, 1) \quad (14)$$

with  $\varepsilon$  being the mean zero random term of the model with cumulative distribution function (CDF)  $F_\varepsilon$ . In this simple setting, the marginal effect of the covariate is constant across quantiles. Note

---

<sup>3</sup>From Mosteller and Tukey (1977): ‘Just as the mean gives an incomplete picture of a single distribution, so the regression curve gives a correspondingly incomplete picture for a set of distributions.’

197 that the result in Equation (14) holds for any distribution of the error term. Quantile regression  
198 can nonetheless accommodate more complicated data generating processes, like for example the  
199 location-scale model where  $\varepsilon$  is replaced by  $\sigma(Z)\varepsilon$ , with  $\sigma(Z) > 0$  and  $\varepsilon \perp Z$ . In this case the  
200 variance of the random term depends on  $Z$  and it can be shown that the estimated slope in the  
201 quantile regression model will be governed by the quantiles of  $\varepsilon$ .

202 All the quantile regression models return as output a prediction at a specific quantile level. For  
203 example, the model with  $\tau = 0.5$  gives the conditional median prediction for each experimental  
204 unit given particular values of the covariates. Predictive accuracy of the conditional median can  
205 be measured through the mean absolute error (MAE) and the root mean square error (RMSE)  
206 between the point predictions and the observed responses. By fitting a model for several values of  
207  $\tau$ , we can also build prediction intervals for new observations  $(y^*, z^*)$  (Davino et al., 2013; Mayr  
208 et al., 2012). For example, if we fit a model on the same data for two quantile levels  $\tau_1 = \delta/2$  and  
209  $\tau_2 = 1 - \delta/2$  (with  $\delta \in (0, 1)$ ), the interval

$$210 \quad \text{PI}_{1-\delta}(z^*) = \left( \hat{Q}_{\tau_1}(Y|Z = z^*), \hat{Q}_{\tau_2}(Y|Z = z^*) \right) \quad (15)$$

211 should contain the observed response value for new data  $(1 - \delta)100\%$  of the time (provided Equa-  
212 tion (10) is true). For example, a 90% prediction interval can be obtained by fitting a model  
213 for  $\tau_1 = 0.05$  and  $\tau_2 = 0.95$ . This prediction model can effectively handle heteroskedasticity or  
214 skewness, since in quantile regression there are no assumptions on the response distribution: using  
215 simulated data Davino et al. (2013) provide examples in which prediction intervals obtained via  
216 quantile regression achieve the nominal levels where ordinary least squares prediction intervals fail.  
217 This is also confirmed theoretically in Zhou and Portnoy (1996): the coverage probability tends to  
218  $1 - \delta$  with an error of  $O(n^{-1/2})$ , as the sample size of the training set  $n \rightarrow \infty$ .

### 219 2.3. Functional quantile regression

220 A large body of literature has been developed in order to translate regression models into the  
221 functional framework. For example, functional GLMs are now well established in the theory, both in  
222 the frequentist and Bayesian approaches (Müller and Stadtmüller, 2005; Crainiceanu et al., 2009).  
223 Quantile regression (Koenker and Bassett, 1978) has also been extended in the functional data  
224 paradigm: first with Cardot et al. (2005), then with Kato (2012) and Yao et al. (2017), the model  
225 has been readapted for the case of functional covariates with scalar response. The model illustrated



226 in [Kato \(2012\)](#) shares the main characteristics with the scalar-on-function regression of [Müller and](#)  
 227 [Stadtmüller \(2005\)](#), except for the assumption that the conditional quantile is a linear function  
 228 of the (centered) covariates. In particular, the conditional quantile of the response is expressed  
 229 as a linear function of the scalar product between the functional data and a coefficient function  
 230  $\beta_\tau(\cdot) \in L^2(T)$ :

$$231 \quad Q_\tau(Y|X) = \alpha_\tau + \int_T X(t)\beta_\tau(t)dt, \quad \tau \in (0, 1). \quad (16)$$

232 The functional nature of the coefficient makes its interpretation less straightforward than in standard  
 233 regression. In the regions where  $\beta_\tau(t) = 0$  any increment in the covariate produces no marginal  
 234 change on the quantile of the conditional distribution  $Y|X$ . On the other hand, if  $\beta_\tau(t)$  is constant  
 235 over a region  $T^* \subset T$  and null elsewhere, then only the region  $T^*$  plays a role in the prediction  
 236 of the conditional quantile. Despite the differences between quantile and linear scalar-on-function  
 237 regression, the same difficulties of the interpretation of the functional coefficients discussed in [James](#)  
 238 [et al. \(2009\)](#) apply. The model can easily accommodate scalar covariates  $z_1, \dots, z_P$  (see for example  
 239 [Yao et al., 2017](#)):

$$240 \quad Q_\tau(Y|X) = \alpha_\tau + \int_T X(t)\beta_\tau(t)dt + \sum_{j=1}^P z_j \gamma_{j,\tau}, \quad \tau \in (0, 1). \quad (17)$$

241 In order to estimate the parameters in Equation (16), both the predictors and the coefficient  
 242 functions are represented in the truncated Karhunen–Loève expansion in Equation (7):

$$243 \quad X_i(t) \approx \sum_{m=1}^M \nu_{im} \psi_m(t), \quad \beta_\tau(t) \approx \sum_{m'=1}^M b_{m',\tau} \psi_{m'}(t).$$

244 Thanks to the orthonormality of the eigenfunctions  $\psi_m$ ,

$$245 \quad \int_T X_i(t)\beta_\tau(t)dt \approx \sum_{m=1}^M \sum_{m'=1}^M \nu_{im} b_{m',\tau} \int_T \psi_m(t)\psi_{m'}(t)dt$$

$$246 \quad = \sum_{m=1}^M \nu_{im} b_{m,\tau}. \quad (18)$$

248 Thus the functional model in (16) becomes a standard quantile regression problem of the form

$$249 \quad Q_\tau(Y|X) = \alpha_\tau + \sum_{m=1}^M \nu_{im} b_{m,\tau}, \quad (19)$$

250 where  $\alpha_\tau$  and  $b_{1,\tau}, \dots, b_{m,\tau}$  are estimated as in Equation (13). The estimated functional coefficient  
251 is then reconstructed by computing

$$252 \quad \hat{\beta}_\tau(t) = \sum_{m=1}^M \hat{b}_{m,\tau} \psi_m(t); \quad (20)$$

253 for a given  $\tau$  the estimated value for the quantile function is obtained by plugging in the estimated  
254 coefficient into (16):

$$255 \quad \hat{Q}_\tau(Y|X) = \hat{\alpha}_\tau + \int_T X(t) \hat{\beta}_\tau(t) dt. \quad (21)$$

256 In this functional principal components regression (FPCR) setting, the number of principal com-  
257 ponents  $M$  to be used as regressors controls the smoothness and the approximation error with  
258 respect to the real images. The choice of  $M$  could be automated by using information criteria or  
259 percentage of variance explained; nevertheless, there is no guarantee that the first  $M$  components  
260 (which explain the most of the variability of  $X$ ) are also able to capture effectively the relationship  
261 between the functional predictor and the scalar response (Febrero-Bande et al., 2017; Delaigle and  
262 Hall, 2012). For this reason, a simple option could be to select  $M$  such that a very large share of ex-  
263 plained variability is represented and then use LASSO regularisation within the quantile regression  
264 model (Belloni and Chernozhukov, 2011; Wang, 2013). The regularisation might produce a different  
265 subset of selected variables across different quantile levels  $\tau$ . Since for each  $\tau$  a different model has  
266 to be fitted, the plug-in estimator  $\hat{Q}_\tau(Y|X)$  is not guaranteed to be monotonically increasing in  $\tau$   
267 as the conditional quantile function  $Q_\tau(Y|X)$  is by construction.

268 It must be considered that the bias introduced by the penalised estimation could harm the  
269 interpretability of the coefficients for each covariate. A way to solve this issue is the post- $\ell_1$  quantile  
270 regression, where LASSO is used only for model selection and then a vanilla quantile regression  
271 model is fitted using only the covariates selected. This approach guarantees better convergence  
272 rates and could reduce the bias (Belloni and Chernozhukov, 2011).

## 273 *2.4. Data analysis workflow*

### 274 *2.4.1. Imaging*

275 The brain images are acquired using structural MRI. This workflow does not depend on any  
276 specific preprocessing stages, except for intersubject registration to an atlas image, such that voxels  
277 from different images are aligned.

278 More transformations can be operated on the structural MR images. For example, the analysis  
279 can be based on tensor-based morphometry (TBM) images. TBM is an image technique that aims  
280 at showing local differences in brain volume from structural imaging. In a cross-sectional setting  
281 (one image for each subject), each image is aligned to a common MRI template called *minimal*  
282 *deformation template* (MDT). The deformation induced by this alignment can be represented by a  
283 function that maps a 3-dimensional point in the template to the corresponding one in the individual  
284 image. The Jacobian matrix of the deformation can be used to inform about volume differences in  
285 terms of shearing, stretching and rotation. The determinant of the Jacobian matrix for each voxel  
286 is then a summary of local relative volumes compared to the MDT: a value greater than 1 indicates  
287 expansion, while a value less than 1 means contraction. Further details about TBM are available  
288 in [Ashburner and Friston \(2004\)](#).

289 In order to reduce the dimensionality of the problem, the voxels outside the brain can be  
290 excluded from the analysis imposing a mask on the images. We used FSL (through its R interface  
291 `fslr`, [Muschelli et al., 2015](#)) to obtain a mask on the template image with smooth boundaries.

#### 292 2.4.2. Basis expansion

293 A common assumption in FDA is that the observed data are a noisy, discretised version of  
294 the true underlying signal function that is of interest in the analysis. In other words, the values  
295 observed at a specific voxel may be contaminated with some measurement error that could have an  
296 impact on the spatial correlation structure within the images. Removing this measurement error  
297 leads therefore then to smoother images, improving the performances of FPCA.

298 For this reason, nonparametric basis expansion techniques such as B-splines or wavelets are  
299 usually employed. The latter are chosen mainly when the underlying function is thought to be  
300 characterised by rapid changes in behavior ([Ramsay and Silverman, 2005](#)); B-splines are instead  
301 preferred for their properties (compact support, unit sum) when less abrupt changes in the function  
302 are expected. In this case, TBM images are already smooth by construction, so we can use B-spline  
303 basis functions with the main aim to obtain a parsimonious representation (under the fairly safe  
304 assumption that the main sources of error have been already removed).

305 In order to get a 3-dimensional basis function, a tensor product of univariate B-spline basis  
306 functions is considered. Denote by  $B_1^{(j)}(t^{(j)}), \dots, B_{Q_j}^{(j)}(t^{(j)})$  the univariate basis functions for the  
307  $j$ -th dimension ( $j = 1, 2, 3$ ). The number of basis functions for each dimension is  $Q_j = l_j + r - 1$ ,

308 where  $l_j$  is the number of knots and  $r$  is the degree of the spline. We now define the set of basis  
 309 functions

$$310 \quad B_{q_1 q_2 q_3}(t^{(1)}, t^{(2)}, t^{(3)}) = B_{q_1}^{(1)}(t^{(1)}) B_{q_2}^{(2)}(t^{(2)}) B_{q_3}^{(3)}(t^{(3)}) \quad (22)$$

311 for  $q_j = 1, \dots, Q_j$ , for  $j = 1, 2, 3$ .

312 In order to derive the projection of each image onto this set of basis functions, we define the  
 313 following matrix of basis functions using the Kronecker product

$$314 \quad \phi = S^{(3)} \otimes S^{(2)} \otimes S^{(1)}. \quad (23)$$

315 where  $S^{(j)}$  is the  $P_j \times Q_j$ -dimensional matrix whose  $q_j$ -th column contains the evaluation of the  
 316 function  $B_{q_j}^{(j)}(t^{(j)})$  at each point  $t^{(j)}$  (for  $j = 1, 2, 3$ ) and  $P_j$  is the number of points for the  $j$ -th  
 317 dimension. The matrix  $\phi$  has dimensions  $P_1 P_2 P_3 \times Q_1 Q_2 Q_3$  (the number of rows is equal to the  
 318 number of voxels and the number of columns is equal to the number of basis functions). Once the  
 319 basis set is determined, this can be used as set of regressors where the original (vectorised) image  
 320 is the response variable. Estimation can be performed via ordinary least squares:

$$321 \quad \hat{x}_i(t) = \sum_{k=1}^K \tilde{c}_{ik} \phi_k(t), \quad (24)$$

322 where  $K = Q_1 Q_2 Q_3$ ,  $\tilde{c}_i$  is the  $K$ -dimensional vector containing the coefficients of the projection  
 323 for the  $i$ -th image and  $\phi_k(t)$  is the  $k$ -th basis function. In compact form, all the  $N$  images are  
 324 represented by the product of the  $N \times K$  coefficient matrix  $\tilde{C}$  and the matrix of basis functions  $\phi$ .  
 325 We center the projected data (equivalent to centering the raw data since the projection is linear).  
 326 This apparently negligible aspect is actually very relevant in the big data context as it allows to  
 327 parallelise the basis expansion stages without the need to import and store simultaneously all the  
 328 images. We call the centered coefficient matrix  $C$ .

329 In this work we used a 3D tensor product of quadratic B-spline univariate basis functions with  
 330 equidistant knots. The number of knots (or analogously their spacing) can be fixed in advance,  
 331 but a poor choice might heavily affect the number of basis functions that are needed to represent  
 332 the functions and consecutively the computational time and the quality of projection. For this  
 333 reason a preliminary study on a subset of the data is recommended. Outcomes of interest for this  
 334 preliminary study could be the number of non-zero basis functions within the masked image, the  
 335 average time needed for the projection of an image and the  $R^2$  value obtained from the regression of  
 336 each image using as design matrix the matrix of basis functions. The latter value can be interpreted

337 as a proportion of variance explained. At this stage, it is highly recommended to retain as much  
 338 variability as possible: a 0.95 threshold for  $R^2$  should work for many applications and should ensure  
 339 a manageable set of basis functions. Alternative criteria could be established in terms of full width  
 340 at half maximum (FWHM).

### 341 2.4.3. Functional PCA

342 The coefficients of the projection are the quantities needed to solve the eigendecomposition prob-  
 343 lem in Equation (8). In this section, we rely heavily on Ramsay and Silverman (2005, Section 8.4.2),  
 344 with minor modifications to make this high dimensional problem computationally feasible. The pro-  
 345 cedure is described also in Chen et al. (2018).

346 The sample variance-covariance function can be written as

$$347 \hat{v}(s, t) = \frac{1}{N-1} \phi(s)^T C^T C \phi(t) \quad (25)$$

348 using the same decomposition in (24). Suppose then that the eigenfunctions in Equation (8) can  
 349 be expressed as linear combinations of the same basis functions  $\phi$ :

$$350 \psi(s) = \sum_{k=1}^K \xi_k \phi_k(s) = \phi(s)^T \xi. \quad (26)$$

351 Then the eigenanalysis of the covariance operator described in Equation (8) takes the following  
 352 form:

$$353 \int_T \left[ \frac{1}{N-1} \phi(s)^T C^T C \phi(t) \right] [\phi(t)^T \xi] dt = \lambda \phi(s)^T \xi. \quad (27)$$

354 Denoting by  $W$  the  $K \times K$  symmetric basis product matrix with elements

$$355 w_{kl} = \langle \phi_k, \phi_l \rangle, \quad (28)$$

356 Equation (27) can be rewritten as

$$357 \frac{1}{N-1} \phi(s)^T C^T C W \xi = \lambda \phi(s)^T \xi. \quad (29)$$

358 The entries in  $W$  are usually computed with some numerical quadrature rules (Ramsay and Sil-  
 359 verman, 2005) but these procedures are computationally demanding in our 3D context. The cross  
 360 product, although less accurate at the boundaries with respect to the trapezoidal rule, offers a good  
 361 result in shorter time. Simplifying both sides of Equation (29) by  $\phi(s)^T$  (the relationship must  
 362 hold for all  $s$ ) we obtain

$$363 \frac{1}{N-1} C^T C W \xi = \lambda \xi. \quad (30)$$

364 In order to get orthonormal eigenfunctions, some constraints must be imposed:

$$365 \quad \xi_i^T W \xi_i = 1 \quad \text{and} \quad \xi_i^T W \xi_j = 0.$$

366 These are fulfilled by setting  $u = L^T \xi$ , where  $L$  is obtained through the Cholesky decomposition  
 367  $W = LL^T$  (Ramsay and Silverman, 2005, p. 181); solving the equivalent problem

$$368 \quad \frac{1}{N-1} L^T C^T C L u = \lambda u, \quad (31)$$

369 the original eigenfunctions are obtained using  $\xi = (L^T)^{-1} u$ .

370 We note that for  $A = (N-1)^{-1/2} CL$  the eigendecomposition problem consists in finding the  
 371 eigenvalues and eigenvectors of  $A^T A$ . These can be obtained in a computational efficient way by  
 372 using the SVD of the matrix  $A$ . In particular, the non-zero eigenvalues  $\lambda$  are equal to the squared  
 373 non-zero singular values, whereas the eigenvalues  $u$  of  $A^T A$  are equal to the right singular vectors  
 374 of  $A$ . The  $m$ -th score for the  $i$ -th image is then

$$375 \quad \begin{aligned} \nu_{im} &= \langle X_i - \mu, \psi_m \rangle \\ &= \int_T \left[ \sum_j c_{ij} \phi_j(t) \right] \left[ \sum_k \xi_{mk} \phi_k(t) \right] dt \\ &= c_i^T W \xi_m. \end{aligned} \quad (32)$$

#### 379 2.4.4. Functional Quantile Regression

380 The scores obtained after FPCA are plugged into a standard quantile regression problem. We  
 381 create the design matrix for the quantile regression model using the first  $M$  scores for each image  
 382 such that the first  $M$  eigenfunctions represent at least 80% of the variability within the sample (see  
 383 Section 4.3 for a sensitivity analysis). LASSO regularisation can be applied within the quantile  
 384 regression framework. The minimisation problem in Equation (13) can be readapted therefore to  
 385 our situation by writing

$$386 \quad (\hat{\alpha}_\tau, \hat{b}_{1,\tau}, \dots, \hat{b}_{M,\tau}) = \arg \min_{\alpha, b_1, \dots, b_M} \left\{ \sum_{i=1}^n \rho_\tau \left( y_i - \alpha - \sum_{m=1}^M \nu_{im} b_m \right) + h_{LASSO} \sum_{m=1}^M |b_m| \right\} \quad (33)$$

389 where  $h_{LASSO}$  is the LASSO tuning parameter. For a specific value of  $h_{LASSO}$ , a solution path is  
 390 found, where the Lasso penalty will induce the shrinkage of the estimates towards zero, but also  
 391 sparsity, as some estimates are exactly zero (Tibshirani, 1996).

392 Several R packages offer built-in functions that perform automatic selection of the tuning param-  
393 eter. For this purpose, we use the package `rqPen` (Sherwood and Maidman, 2017), that produces  
394 penalized quantile regression models for a range of tuning parameters and then selects the one with  
395 minimum cross-validation error.

#### 396 *2.4.5. FPCA and functional quantile regression in a prediction setting*

397 The scores are obtained by taking an inner product of each image with the eigenfunctions  
398 estimated on the training set. For this reason, they can be obtained for images from other datasets  
399 with the same formula, even if the properties of zero mean and variance equal to the eigenvalues  
400 apply only for the training dataset. The scores are in turn produced within the FPCA step, where  
401 the estimation of the eigenfunctions depends on the training data as well.

402 This workflow is aimed at deriving brain age prediction intervals for healthy individuals. This  
403 means that FPCA and functional quantile regression should be based on a dataset of control  
404 subjects. In order to get predictions for this dataset, 10-fold cross validation can be used, reducing  
405 in this way the risk of overfitting. Age predictions for subjects with neurodegenerative diseases can  
406 be obtained from the same normative model. In this case the full dataset of control subjects can  
407 be used for FPCA and functional quantile regression and the brain age is to be interpreted as the  
408 equivalent brain age of a healthy individual having the same brain image.

409 The R code implementing the workflow is available at [https://github.com/marcopalma3/](https://github.com/marcopalma3/neurofundata)  
410 [neurofundata](https://github.com/marcopalma3/neurofundata).

#### 411 *2.4.6. Alternative models*

412 The degree of smoothing in the basis expansion step can be controlled in different ways, by  
413 changing either the location or the numbers of knots. When the number of knots is equal to the  
414 number of voxels, we recover the original data, where the coefficient of the basis functions are just  
415 the observed values at each voxel. The analysis of the “unsmoothed” images can still be based on  
416 standard multivariate analysis techniques such as PCA and quantile regression, but it requires an  
417 increased computational effort. The data matrix containing the images as rows is indeed large (in  
418 our case the memory needed to store it is more than 6.4GB) and high performance computing tools  
419 are required to fit models on these data. In addition, quantile regression under memory constraints  
420 is receiving attention only recently (Chen et al., 2019), therefore the calculation of the prediction

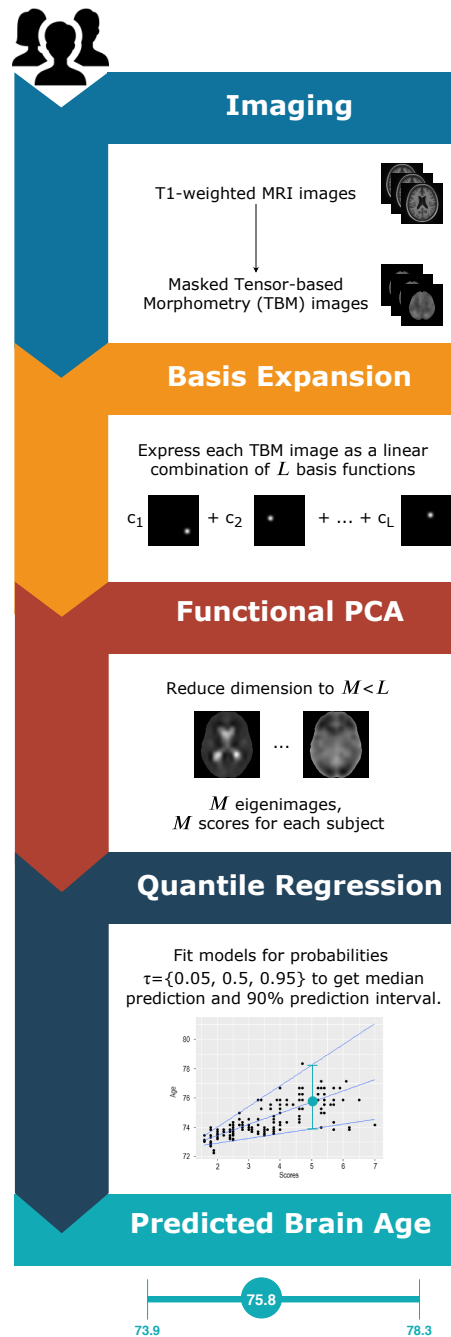


Figure 1: Flowchart of the analysis from the brain images to the predicted intervals.



421 interval is not straightforward. A small amount of smoothing is recommended to reduce both the  
422 storage issues and the computational time required to train the model.

### 423 3. Data

424 The workflow proposed in Section 2.4 is applied on a dataset coming from the Alzheimer's  
425 Disease Neuroimaging Initiative (ADNI, [Mueller et al., 2005](#)), that supports the investigation about  
426 biological markers to be used to detect Alzheimer's Disease (AD) at early stages. The sample used  
427 in this paper is made of 796 subjects, identified through an ID code, for which several demographic  
428 and clinical variables are measured. In this analysis, we will consider only the chronological age at  
429 the entry of the study (ranging from 59.90 to 89.60 years; mean age  $75.60 \pm 6.29$ ) and their diagnosis:  
430 180 subjects were diagnosed with AD, 387 with MCI (Mild Cognitive Impairment, considered as an  
431 intermediate stage between healthy condition and AD) and 229 people were belonging to a control  
432 group of cognitively normal (CN) subjects. The histogram of age by diagnosis group is displayed  
433 in Figure 2.

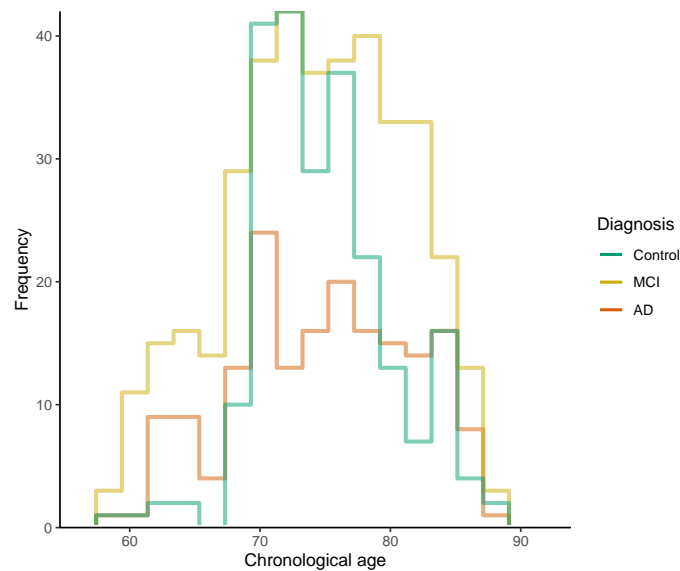


Figure 2: **Histogram of age of the subjects in the sample, for each diagnosis.** The number of bins has been fixed using the Freedman-Diaconis rule ([Freedman and Diaconis, 1981](#)).

434 The functional part of the dataset consists of tensor-based morphometry (TBM) images taken

Diagnosis	$N$	Min.	1st Qu.	Median	Mean	3rd Qu.	Max.
Control	229	59.90	72.30	75.60	75.87	78.50	89.60
MCI	387	60.10	70.85	75.60	75.30	80.40	89.30
AD	180	59.90	70.98	76.15	75.90	81.58	89.10

Table 1: **Summary statistics for each diagnosis group.**  $N$  is the number of subjects in each group. The second part of the table shows selected quantiles of age.

435 at the baseline of the study for each subject. In this dataset, the threshold 1 is rescaled to 1000 for  
436 computer number format reasons. Information about the preprocessing stages for the ADNI TBM  
437 dataset is available in [Hua et al. \(2013\)](#).

438 The analysis is based on the original 3D TBM scans ( $220 \times 220 \times 220$ , with voxel size equal to  
439  $1 \text{ mm}^3$ ). The conventional neurological orientation (“right is right”) is used: the  $(x, y)$  axes of the  
440 images are set such that  $x$  increases from left to right and  $y$  increases from posterior to anterior.

441 The mean functions for each diagnosis are shown in Figure 3. MCI and AD patients share  
442 similar average brain volumes patterns (namely, expansion of the lateral ventricles and shrinkage  
443 almost everywhere else) even if the intensity of the expansion is higher for people with dementia.  
444 The expansion of the lateral ventricles is also visible in the healthy control mean function, but it  
445 is less pronounced. Conversely, the healthy control mean function shows other slightly expanded  
446 brain areas, such that the cerebellum and several regions in the posterior and frontal lobes. Further  
447 analyses based on the voxelwise variance functions per each group show that the lateral ventricles  
448 are the areas with the highest variability in terms of volume expansion.

## 449 4. Results

### 450 4.1. Prediction accuracy

451 The preprocessed images are masked to remove unnecessary voxels for the analysis. A 3D smooth  
452 mask is obtained by smoothing the raw mask with a Gaussian kernel with standard deviation equal  
453 to 2 voxels (FWHM 4.7 mm) and thresholding it at 0.5, to regularise the boundary, producing just  
454 over 2 million nonzero voxels.

455 For the dataset at hand the B-splines projection with equidistant knots every 12 mm (equivalent  
456 to FWHM  $\approx 15.33$  mm) for each dimension allows to represent each image with  $R^2$  approximately

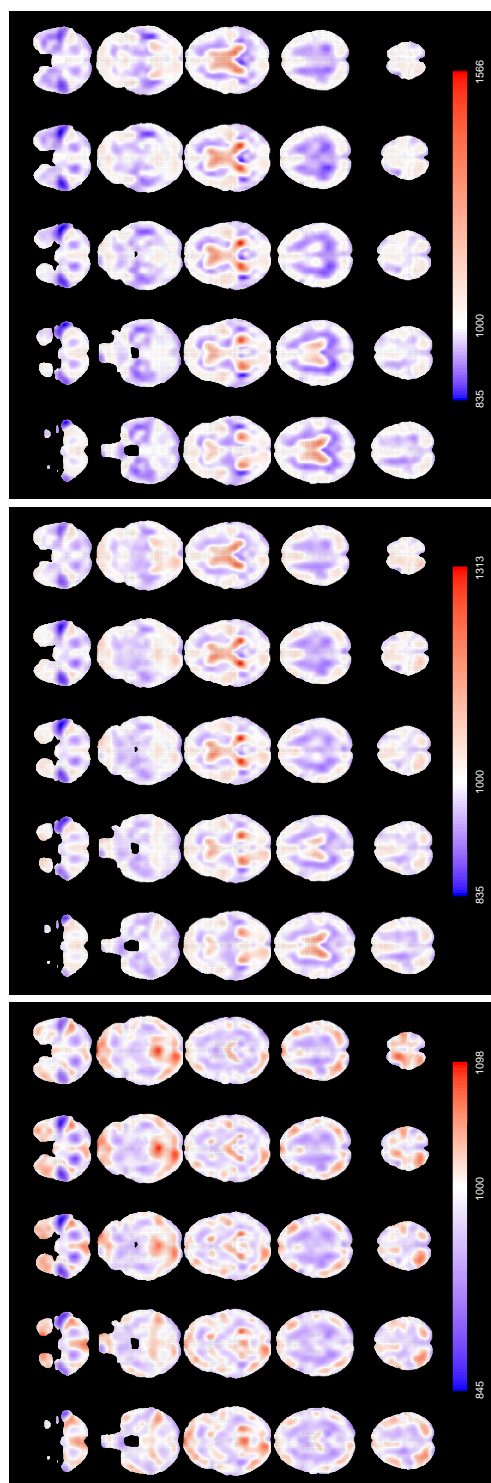


Figure 3: Axial slices of the mean images for each diagnosis (from left to right: Control, MCI, AD). Slices are ordered from bottom to top. The colours are overlaid on the corresponding slice of the MDT.

457 equal to 0.96. The number of B-spline functions in the tensor product that fall within the mask is  
458 2694. In the current implementation, the process of importing one image into R and obtaining its  
459 B-spline coefficients takes approximately 30 seconds.

460 The eigendecomposition problem in Equation (8) solved for the dataset of healthy control sub-  
461 jects returns  $M = 54$  eigenfunctions of which the first 3 are plotted in Figure 4. In analogy with  
462 standard PCA, a basic interpretation can be provided. The first eigenfunction clearly distinguishes  
463 the lateral ventricles from the rest of the brain. Subjects with high scores for this eigenfunctions  
464 will show stronger expansion within the lateral ventricles with respect to the mean function. Due  
465 to the similarities with the observed patterns in the mean function for the subjects with disease, it  
466 is likely that the scores for this eigenfunction computed for all the 796 subjects in the dataset are  
467 correlated with the diagnosis and with the chronological age, for the known interplay of the effects  
468 of these two factors. The second mode of variation refers instead to a more general expansion across  
469 the whole brain: in other words, it discriminates between individuals with bigger brains and those  
470 with smaller ones. For this reason, this component might account for some sex-related effects, as  
471 males have on average larger overall absolute brain than females (Ruigrok et al., 2014). The third  
472 eigenfunction weights negatively some of the internal parts of the brain. This component might  
473 therefore roughly distinguish white matter from the cortex, even if this interpretation is not very  
474 clear and can be influenced by the smoothing induced by the projection onto the basis functions.  
475 The first 3 components account for 36.25% of the variance of the images of the healthy control  
476 group.

477 We compute the scores for MCI and AD individuals as the product of the centered images and  
478 the eigenfunctions in Figure 4. For the control subjects, we use 10-fold cross validation (with check  
479 function as loss function) to run FPCA, produce scores and fit the models such the predictions  
480 are obtained on held-out data. Quantile regression models for  $\tau \in \{0.05, 0.5, 0.95\}$  are considered.  
481 Table 2 shows that the MAE and RMSE based on the difference between median brain-predicted  
482 age and chronological age are lower for control subjects than the other groups. This result is  
483 expected under the choice of a normative model that predicts brain age in absence of any diseases  
484 and indicates that the two subpopulations (controls vs. cases) show different ageing characteristics  
485 (if they were belonging to the same population, the MAE and RMSE would have been similar).

486 The MAE observed for the control group is 3.49, in line with other results obtained in the  
487 literature for other MRI datasets and different age ranges (Cole et al., 2019). In addition, as shown

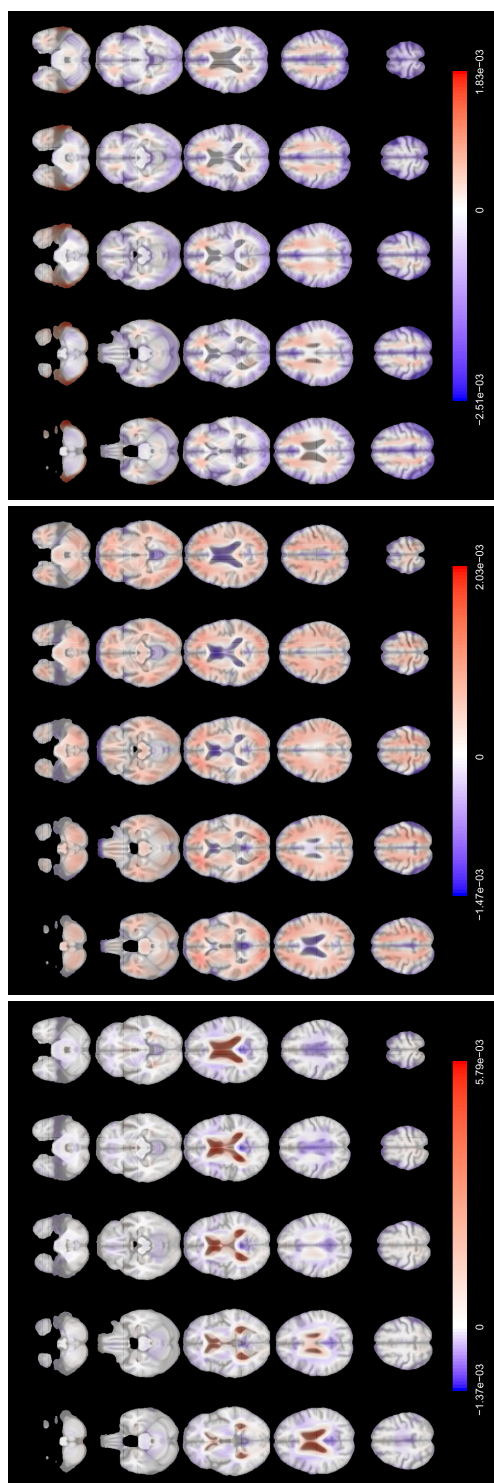


Figure 4: Axial slices of the first 3 eigenfunctions for the control subset. Slices are ordered from bottom to top. The colours are overlaid on the corresponding slice of the MDT. The eigenfunctions account respectively for 15.43%, 13.95%, 6.87% of the total variability. The signs of the eigenfunctions are determined on the basis of clinical interpretation.

Diagnosis	$N$	MAE	RMSE	Cor	95% $CI_{Cor}$	$\hat{\pi}$	*-pos
Control	229	3.49	4.43	0.48	[0.37, 0.57]	0.86	0.05
MCI	387	4.99	6.12	0.46	[0.38, 0.54]	0.68	0.24
AD	180	5.16	6.27	0.38	[0.25, 0.50]	0.64	0.28

Table 2: **Summary of the prediction results by diagnosis.** Cor: correlation between predicted brain age and chronological age.  $CI_{Cor}$ : confidence interval for the correlation between predicted brain age and chronological age, obtained via Fisher-z transformation (Myers et al., 2013, Section 19.2).  $\hat{\pi}$ : sample coverage (proportion of cases for which the 90% prediction interval contain the chronological age). \*-pos: proportion of cases for which the chronological age is less than the lower limit of the 90% prediction interval.

488 in Figure 5, the smoothed regression line for control subjects indicates that the average *brainPAD*  
 489 (difference between predicted and chronological age) is close to zero for the whole age range, while  
 490 it departs from it for the other groups in the predicted age range between 73 and 75. Prediction  
 491 metrics do not improve after debiasing using post- $\ell_1$  quantile regression.

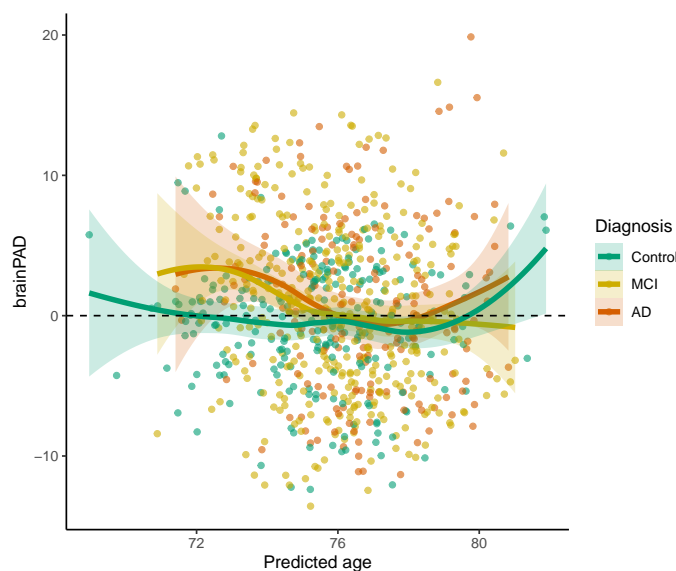


Figure 5: **Plot of the brainPAD vs. predicted response.** The coloured lines are local regression lines obtained with `loess` (locally estimated scatterplot smoothing) with `span = 0.75` and 95% confidence bands.

492 We focus now our attention on the features of the 90% prediction intervals and the sample  
 493 coverage. We observe that the actual sample coverage for control subjects is slightly lower than

494 the nominal level. The groups with cognitive impairment show lower coverage with respect to the  
495 control group: the chronological ages of around 1 in 3 subjects with diseases do not fall in the  
496 prediction intervals obtained under the normative model. When we further analyse the direction  
497 of the discrepancy, we can define a “\*-positive brainPAD” group (for which the chronological age  
498 is lower than the lower limit of the prediction interval, or equivalently with positive brainPAD and  
499 chronological age outside the prediction interval) and a “\*-negative brainPAD” one (composed of  
500 those subjects with negative brainPAD and chronological age outside the prediction interval). While  
501 the share of \*-negative subjects is approximately constant across the diagnosis, the percentage of \*-  
502 positive subjects for MCI and AD groups is approximately 5 times the one for the control subjects.  
503 This result aligns with the literature, where it has been shown that MCI and AD patients show  
504 higher apparent brain age (Cole et al., 2019; Franke et al., 2012): for this reason the \*-positive group  
505 is more interesting for their potential correlation with other disease indicators. All the prediction  
506 intervals are plotted in Figure 6, stratified by diagnosis and sorted by predicted age. The prediction  
507 intervals for the control subjects are scattered closer to the line of identity between predicted and  
508 chronological age and there are no relevant trends in the residuals that are left unexplained by  
509 the regression models. The variability of the width of the 90% prediction intervals is displayed in  
510 Figure 7: the average width is similar for the 3 diagnosis groups, but there is higher variability in the  
511 width distribution of the MCI and AD subjects. Moreover, \*-positive brainPAD is mainly observed  
512 in the lower part of the age domain covered in the dataset. This could be just a consequence of  
513 our regression approach, or it might be due to the low number of subjects in the training set with  
514 chronological age less than 70, which might produce issues in the estimation of extreme quantiles  
515 of the conditional distribution of the outcome.

516 The brain maps displayed in Figure 8 are the functional coefficients obtained from the scalar-  
517 on-image quantile regression trained on the whole control dataset. They can be used to identify  
518 the regions that are responsible for the age prediction for the different quantiles. The functional  
519 coefficient for  $\tau = 0.05$  shows that the expansion of the lateral ventricles is the principal factor that  
520 leads to higher predicted age (Preul et al., 2006; Apostolova et al., 2012) in the lower tail of the  
521 chronological age distribution. Other areas seem to have more limited impact on the prediction.  
522 In the coefficient obtained from the median regression, the lateral ventricles still play a role in  
523 the prediction (especially the posterior part) but expansion in several other areas is correlated to  
524 higher predicted age. Among them we point out the central sulcus (perpendicular to the median

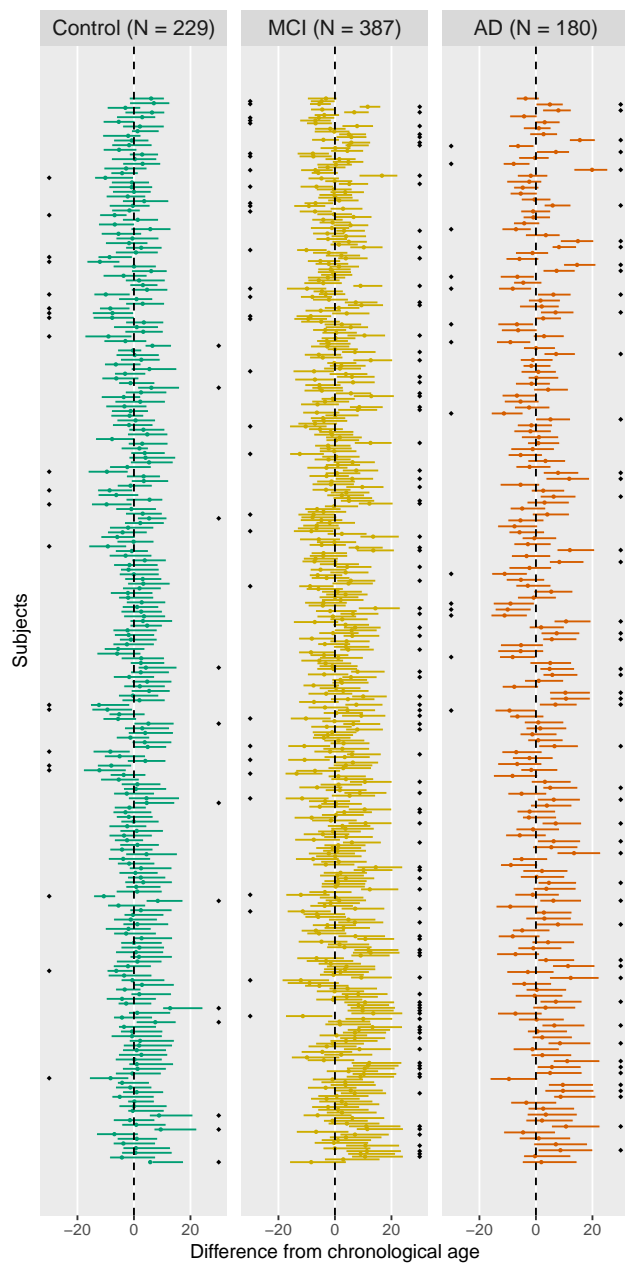


Figure 6: **Brain age 90% prediction intervals, relative to chronological age.** There is one interval per subject, and subjects are sorted in descending order of predicted brain age (higher predicted ages at top). The black diamonds indicate the subjects for which chronological age does not fall into the prediction interval; the side indicates if the subject is in the \*-negative (diamonds on the left) or \*-positive group (diamonds on the right).



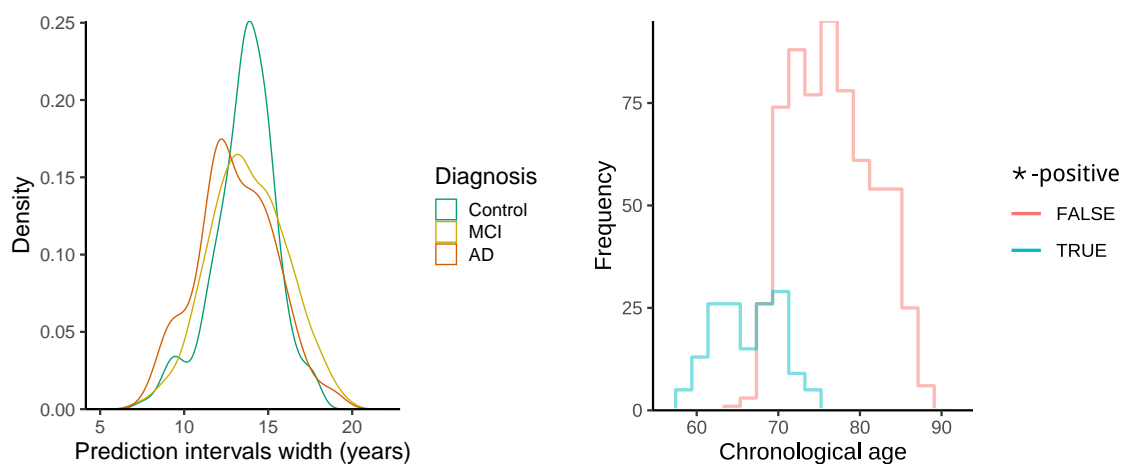


Figure 7: **Left:** distribution of the prediction interval width conditioned by diagnosis. **Right:** histogram of chronological age conditioned by \*-positive indicator (equal to 1 if the chronological age is less than the prediction at  $\tau = 0.05$ , 0 otherwise).

525 longitudinal fissure that divides the two hemispheres) that separates the primary motor cortex  
526 and the primary somatosensory cortex. In addition, the frontal lobe shows negative values for the  
527 functional coefficient, meaning that expansion in this part of the brain is linked to a lower predicted  
528 age. This agrees with the literature: age-related atrophy is more pronounced in the frontal lobe  
529 (Fjell et al., 2014; Cabeza and Dennis, 2013; MacPherson and Cox, 2017) and less in the occipital  
530 lobe (Dennis and Cabeza, 2011). For  $\tau = 0.95$ , the brain map indicates that the upper part of  
531 the cortex and the cerebellum are related to higher predicted age, while a larger left temporal lobe  
532 (in blue in the lower axial slices, it plays a role in memory and language control) is associated to  
533 younger brain age. Especially for these last two maps, asymmetry between hemispheres appears in  
534 the relationship with brain age.

#### 535 4.2. Correlation with cognitive decline measures

536 A small number of cognitive decline measures available in ADNI has been used to evaluate the  
537 clinical utility of the predictions obtained. The list of measures reported in Table 3 includes genetic  
538 assessments (ApoE4) and various evaluations of writing and speaking skills, visual attention and  
539 task switching. The outcomes of interest in this section are both the brain-predicted age difference  
540 (*brainPAD*, difference between predicted and chronological age, as defined in Cole et al., 2017) and  
541 the binary \*-positive indicator (equal to 1 if the chronological age is less than the prediction at

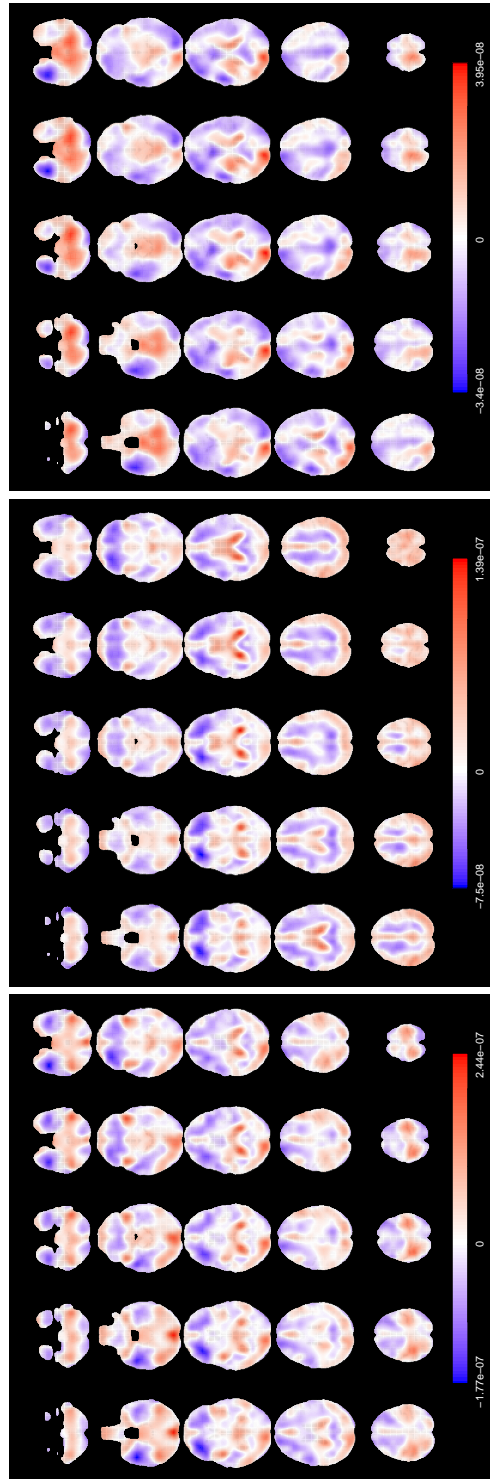


Figure 8: Axial slices of the functional regression coefficient for  $\tau = \{0.05, 0.5, 0.95\}$  (from left to right). Slices are ordered from bottom to top. The colours are overlaid on the corresponding slice of the MDT. For a unit increase (expansion) in the observed TBM image in a red voxel, there is an increase in predicted brain age, while in a blue voxel there is a decrease.

542  $\tau = 0.05$ , 0 otherwise).

Variable		Values	
ApoE4	Apolipoprotein E - Number of $\epsilon 4$ alleles	{0, 1, 2}	↗
ADAS11	AD Assessment Scale - 11-item variant	{0, 1, ..., 70}	↗
ADAS13	AD Assessment Scale - 13-item version	{0, 1, ..., 85}	↗
ADASQ4	AD Assessment Scale - Delayed Word Recall	{0, 1, ..., 10}	↗
MMSE	Mini-Mental State Examination	{0, 1, ..., 30}	↘
DIGITSCOR	Digit Symbol Substitution Test	{0, 1, ..., 83}	↘
TRABSCOR	Trails B Making Test	{0, 1, ..., 996}	↗

Table 3: **Cognitive decline measures used in the analysis.** The arrows indicate the change in the measures associated to an increase in dementia severity.

543 Figure 9 summarises the main findings in this validation analysis. A higher ApoE4 value—  
 544 linked to higher risk of dementia—is also related to higher predicted age difference on average (the  
 545 p-values refer to one-sided tests). In addition, for the group with the highest ApoE4, more than  
 546 75% of the individuals show higher predicted age than chronological.

547 The correlation between baseline *brainPAD* and cognitive scores at different visits shows some  
 548 association (uncorrected) for several measures, with ADAS measures and MMSE showing the  
 549 strongest associations after 2 years. Nevertheless, no cognitive measure recorded at baseline is  
 550 associated with the difference between predicted and chronological age. On the other hand, there is  
 551 some evidence that the average of the cognitive measures is different between the \*-positive group  
 552 and the rest of the subjects across different time points. Also in this case the direction of the  
 553 relationship is consistent with the numerical definition of the measures.

#### 554 4.3. Sensitivity analysis

555 The prediction results are obtained under specific choices of several parameters. In order to  
 556 assess how these choices might affect the results, we perform a sensitivity analysis using different  
 557 values of the following parameters:

- 558 • PVE: proportion of variance explained (criterion to decide the number of fPC to be included  
 559 in the quantile regression models),  $PVE \in \{0.65, 0.8, 0.95\}$ ;

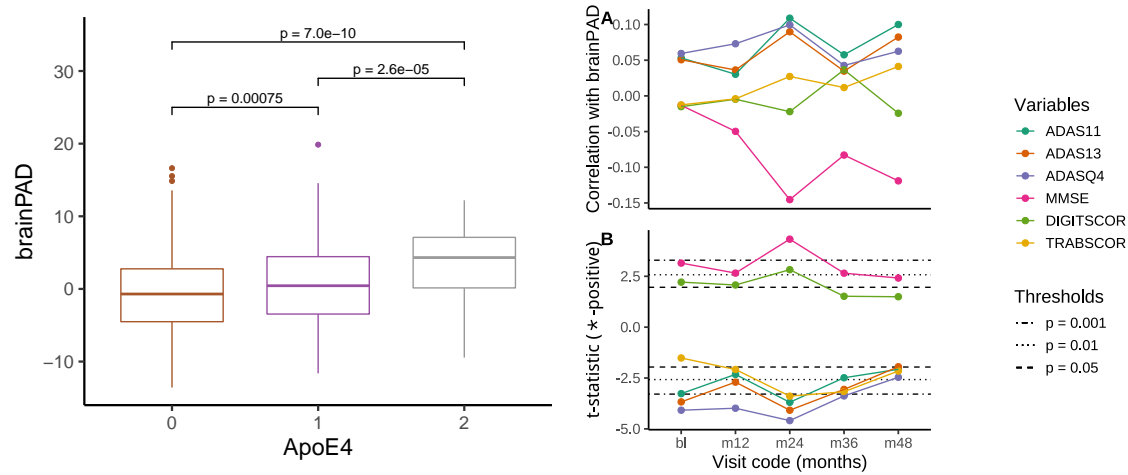


Figure 9: Left: association of *brainPAD* with ApoE4 value (Holm-corrected p-values) for different visits, with evidence of positive association. Right: (A) Correlation between baseline *brainPAD* and cognitive scores at different visits; (B) t-statistic for the comparisons of means of cognitive scores between \*-positive group and the rest of the sample at different visits. The black lines are Student's t quantiles which correspond to different probabilities in the tails of the distribution.

- 560 • KS: knot spacing,  $KS \in \{6, 9, 12, 15\}$ ;
- 561 • nominal coverage: desired width of the prediction intervals. Values considered:
  - 562 –  $\tau \in \{0.1, 0.5, 0.9\}$  for a 80% nominal coverage,
  - 563 –  $\tau \in \{0.05, 0.5, 0.95\}$  for a 90% nominal coverage.

564 For each combination of values, we get the projections for each image and then fit the LASSO  
 565 quantile regression. For the cases with  $KS = 6$ , the standard procedure did not work because of  
 566 a failure in the Cholesky decomposition of the weight matrix  $W$  in Section 2.4, due to numerical  
 567 tolerance issues. In these cases, the pivoted Cholesky decomposition can be applied: due to the  
 568 fact that the matrix  $W$  is symmetric semipositive definite by construction, there is a permutation  
 569 matrix  $P$  for which  $P^T W P$  can be factorised with an upper triangular matrix (see Higham, 2009  
 570 for an introduction).

571 We report as main outcomes the mean absolute error and the actual relative coverage ( $1 - h$ ,  
 572 where  $h$  is the ratio between observed and nominal coverage) obtained for the control subjects in  
 573 Figure 10.

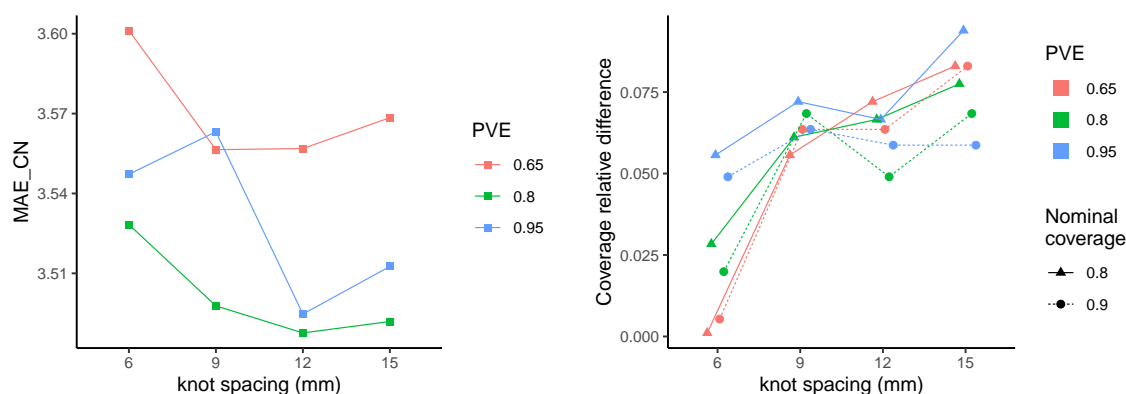


Figure 10: **Left:** mean absolute error for control subjects as function of proportion of variance explained and knot spacing. **Right:** Coverage relative difference of prediction intervals induced by each choice of proportion of variance explained, knot spacing and nominal coverage. Points are jittered horizontally for visualisation purposes.

574 The MAE refers to the predictions obtained with  $\tau = 0.5$ , so it is not affected by the choice of  
 575 nominal coverage. In general, the MAE remains rather stable across combinations of PVE and knot  
 576 spacing, suggesting that our results are robust to the choices of these parameters. The lower MAE  
 577 is always achieved for  $PVE = 0.8$ : this might suggest that a low PVE neglects important sources of  
 578 variation while a higher one introduces too many useless variables in the models. In terms of knot  
 579 spacing, 12 mm gives in almost all the cases the best results across PVE values.

580 Looking at the coverage for each setting of knot spacing, PVE and nominal coverage, we first  
 581 observe that there are no cases in which the observed coverage is higher than the nominal level. This  
 582 phenomenon of undercoverage gets more pronounced for higher knot spacing values. Except for  
 583  $KS = 6$ , when the coverage relative difference increases as the number of components in the quantile  
 584 regression increases, for the other KS values no clear pattern is visible. The relative difference seems  
 585 not to be influenced by the prespecified nominal coverage.

586 The table in the Supplementary Material section includes also a sanity check based on non-  
 587 monotonic prediction intervals - those for which the predicted age at the upper  $\tau$  level is smaller  
 588 than the one at the lower level. The number of occurrences of this phenomenon is negligible in  
 589 almost all the cases.

590 As an additional analysis, we have explored the prediction performances in terms of MAE for  
 591 the control group in two models which do not use the basis expansion step, using the R packages

592 `bigmemory` (Kane et al., 2013) and `bigstatsr` (Privé et al., 2018). The first model (M1) is a sparse  
593 linear regression with LASSO regularisation applied on the unsmoothed data (represented by 1  
594 column per voxel in the data matrix). The second model (M2) is closer to our approach: a PCA  
595 is performed on the covariance of the matrix of unsmoothed images, then the scores corresponding  
596 to the first principal components selected (using a proportion of variance explained of at least 0.8)  
597 are plugged into a penalised quantile regression model. M2 can be interpreted as a special case of  
598 our functional approach when the distance between adjacent knots is equal to 1 mm.

599 The difference in computational time between our approach (M0) and the models M1 and M2 is  
600 not substantial. On one hand, the smoothing step in M0 is performed independently for each image  
601 in a parallelised setting therefore it requires only a few minutes in total. On the other hand, M1  
602 and M2 require to load the matrix (6.4 GB in our case) in memory and run sparse linear regression  
603 or PCA and quantile regression which could take several minutes. For what concerns the prediction  
604 performances, M0 achieves lower MAE for the control group with respect to M1 (MAE = 3.63) and  
605 M2 (MAE = 3.65).

## 606 5. Discussion and further research

607 The functional data paradigm represents a useful approach to the analysis of complex data  
608 such as brain scans and offers a way to fit a global model for 3D images. In this work we have  
609 discussed the basic aspects of functional data and presented an application of quantile scalar-on-  
610 image regression (as extensions of classical quantile regression) in the field of brain age studies.  
611 Following the existing literature, we have devised an efficient workflow that takes as input a tensor-  
612 based morphometry image and returns a prediction interval. The advantages of employing the  
613 whole images as covariates are that some common preprocessing steps might be avoided (e.g. brain  
614 tissue segmentation) and there is no need to summarise information at the ROI (regions of interest)  
615 level. In addition, quantile regression gives a more detailed picture of the relationship between the  
616 covariate and the response and returns an interval with the desired coverage when the distribution of  
617 the dependent variable departs from normality. In contrast with other existing models coming from  
618 a machine learning perspective, our method outputs not only a point estimate but also a prediction  
619 interval. In addition, the model allows to investigate the functional coefficient estimated, in order  
620 to visualise the brain regions that influence most the predicted age.

621 Our modelling strategy introduces new features with respect to the standard prediction-oriented  
622 approaches in the literature. While other approaches focus only on maximising prediction accuracy,  
623 we emphasise the detection of individual atypical ageing: the prediction intervals give a simple  
624 and preliminary assessment of the relevance of the observed brainPAD. In other words, the same  
625 brainPAD could be indicative of potential neurodegenerative diseases for one subject, while being  
626 less linked to such disease for another subject.

627 The results from the analysis of ADNI data are encouraging: the point (median) prediction per-  
628 formances in terms of MAE and RMSE for the control subjects are comparable with the literature  
629 on the topic—even with deep learning approaches applied on bigger ADNI datasets ([Varatharajah  
630 et al., 2018](#))—while being also more principled and interpretable. The correlation between chrono-  
631 logical and predicted age results to be lower than the one found with other methods. The model  
632 trained on the control group highlights differences with respect to the MCI and AD groups: indi-  
633 viduals with cognitive impairment are predicted to be older on average than their observed age, as  
634 observed in the literature ([Cole et al., 2017](#); [Franke et al., 2012](#)).

635 The model proposed is an example of penalised functional regression. In this respect, some  
636 degree of regularisation can be applied at different stage of functional data analysis, starting from  
637 smoothing ([Ramsay and Silverman, 2005](#)). At the same time, the choice of the number of functional  
638 principal components to be used in regression (by using the proportion of variance explained) is itself  
639 a penalisation. On top of this we added a further penalisation, driven this time by the relationship  
640 between outcome and predictors, to account for the potential high number of covariates given the  
641 sample size (following the indication provided in [Heinze et al., 2018](#)). Our model represents a  
642 novelty in the literature as it easily accommodates this aspect into a quantile regression model with  
643 3D functional covariates.

644 In addition to the bias induced by the regularisation, another potential issue related to the  
645 functional coefficient is its sensitivity to the modelling strategy used. As extensively studied in  
646 [Happ et al. \(2018\)](#), the smoothness induced by splines could lead to different estimates with respect  
647 to other approaches (e.g. wavelet basis expansion or random field methods). Further work can  
648 be done to confirm the contribution of each brain region to the final prediction. Nevertheless, the  
649 predictive ability - which is the first focus of our model - does not seem to be harmed by this  
650 modelling choice.

651 Our approach is competitive in terms of speed compared to existing methods ([Franke et al.,](#)

652 [2012](#); [Cole, 2017](#)). In particular, for a new image the model returns the predicted interval in  
653 approximately a minute and the training phase of the model is expected to be shorter and less  
654 computationally intensive than training a neural network, especially because the basis expansion  
655 step runs in parallel for each image.

656 The modelling approach illustrated in this paper can be extended in multiple ways, from both  
657 theoretical and practical perspectives. For what concerns the key points of the workflow, in this  
658 paper we have chosen to project the images (and the functional coefficients) using B-spline basis  
659 functions and sketched a possible strategy to select knot spacing. We have shown that some degree  
660 of smoothing produces slightly better predictions with respect to no smoothing at all with negligible  
661 computational cost. The benefit of this approach could more easily appreciated when the number  
662 of images is much larger, in which case loading the whole unsmoothed data into memory can be  
663 unfeasible.

664 The quantile regression approach is a technically easy-to-implement strategy to build prediction  
665 intervals without assuming normality. Since we consider only the best fit for each of the regression  
666 models, it could be of interest to study how the uncertainty about the coefficients and the models  
667 could play a role in the calculation of individual prediction intervals. The observed coverage in the  
668 control group could also depend on the bias/variance trade-off introduced by the cross-validation  
669 procedure (and in particular on the type of penalty and the number of folds chosen). Further  
670 simulation study can be done to assess the extent of this relationship.

671 In addition, further extensions of quantile regression could be considered. Additive terms might  
672 be introduced in order to explore nonlinear effects of the imaging covariate. Moreover, quantile  
673 boosting ([Mayr et al., 2012](#)) could provide better prediction intervals by reducing the bias due to  
674 the estimation at extreme quantiles. This approach has a higher computational cost but keeps the  
675 advantage of interpretability, which is no longer available with other approaches such as quantile  
676 regression forests described in [Meinshausen, 2006](#). A potential issue for the current formulation of  
677 our approach is the phenomenon of *quantile crossing*, that occurs when the predicted quantiles are  
678 not monotonically increasing in  $\tau$  as the conditional quantile function is by construction. Although  
679 in 90% prediction intervals the problem arises rarely (in our application it has been reported for  
680 only 1 case out of 796), still this could introduce some bias. Monotonicity can be forced after the  
681 estimation by using rearrangement or isotonic regression (see e.g. [Kato, 2012](#); [Chernozhukov et al.,](#)  
682 [2010](#)). An alternative modelling strategy for quantile regression that ensures monotonicity of the



683 function is provided in [Chen and Müller \(2012\)](#): the quantile function is obtained indirectly by first  
684 estimating the entire CDF of the response variable and then inverting it to recover the quantile  
685 function at the level of interest. The key idea is to use a generalised functional linear model to  
686 model the conditional distribution of  $Y|X$  as conditional expected values of indicator functions.  
687 This “indirect” model is claimed to provide better estimation of the quantile function with respect  
688 to the classical quantile regression at extreme quantile levels for non-gaussian response variables  
689 ([Chen and Müller, 2012](#)), although the flexibility induced by considering different predictors at  
690 different quantile levels is lost. In addition, generalised additive models for location, scale and shape  
691 (GAMLSS, [Rigby and Stasinopoulos \(2005\)](#)) can also provide a detail picture of the conditional  
692 distribution of the outcome of interest. In GAMLSS the parameters of the distribution (not only the  
693 location, as in GLM) can be written as (smooth) functions of the covariates. GAMLSS can handle  
694 functional covariates ([Brockhaus et al., 2018](#)) and ensures monotonicity of the quantile predictions,  
695 but the family of the conditional distribution of the outcome must be specified in advance.

696 From the application point of view, it is currently very difficult to provide a sensible comparison  
697 between different models. This is due to the large range of possible approaches (from multivariate  
698 statistics to deep learning) applied to a plethora of datasets with different sizes, age ranges and  
699 imaging modalities (T1-weighted MRI to PET or FMRI). [Cole et al. \(2019\)](#) uses a MAE weighted by  
700 the age range in the training set as a measure of comparison. That approach might be too simplistic,  
701 as a 1-year absolute error for a 6-year child should probably be weighted more than the same error  
702 for a 70-year old individual. A more adaptive measure should be devised, or alternatively there  
703 should be an incentive towards the use of a specific dataset as a benchmark. Big databases such as  
704 UK Biobank ([Sudlow et al., 2015](#)) seem the right testing ground for all the methods available in the  
705 literature. Our model could be applied on different imaging modalities, for example voxel-based  
706 morphometry, in order to specify potential differences in the effects due to white and gray matter.

707 Coming to more specific modelling-related issues, as observed from the plots concerning the  
708 prediction intervals, a non negligible correlation is noticed between chronological age and the brain  
709 age differences (predicted minus chronological, called *brainPAD* in [Cole et al., 2017](#), *brainAGE* -  
710 brain age gap estimate - in [Franke and Gaser, 2019](#) or  $\delta$  in [Smith et al., 2019](#)). This undesirable  
711 effect arises from the simple fact that by construction the residuals (which become the objects of  
712 interest when we want to explore the relationship with other variables such as disease conversion) in  
713 a regression model are uncorrelated with respect to the predicted values, but not with the observed

714 ones. Similar issues are also reported in the deep learning approaches to brain age prediction  
715 (Cole et al., 2017; Varatharajah et al., 2018). The work by Smith et al. (2019) identifies potential  
716 reasons for this phenomenon and proposes some solutions. Among others, a viewpoint that is  
717 conceptually grounded and at the same time can be embedded in our model could be rephrasing  
718 the whole problem in terms of a errors-in-variables framework. In particular, this accounts for the  
719 imaging covariate (consistently with the functional data perspective) or its scores representation  
720 being measured with some errors. At the same time, the response itself (chronological age) can be  
721 considered as a noisy proxy for biological brain age (for which it is difficult or even impossible to  
722 define a reference measure).

723 Another aspect left for future research is to extend the analysis of the clinical utility of the  
724 prediction intervals obtained with our workflow by using a larger battery of cognitive measures.  
725 The first basic measures selected in this work show interesting and sensible results, especially for  
726 the correlation with the \*-positive binary variable. A desired feature of this indicator in a prognostic  
727 context should be its correlation with conversion to dementia, in order to provide a sensible way  
728 to early detect neurodegenerative diseases. Furthermore, a similarly defined “\*-negative indicator”  
729 could be also explored in the same way in order to show potential aspects of a healthy aging process.

730 In addition, introducing other covariates in the model (such as sex, years of education or physical  
731 activity measures) is rather straightforward and it could improve the detection of discrepancies from  
732 normative ageing. On the other hand, these covariates might potentially introduce confounding  
733 effects: the variability due to non-imaging information could be already captured by one or more  
734 functional principal components. Our approach can be also easily incorporated in a longitudinal  
735 model where brain age trajectories could provide evidence of stable or accelerated brain ageing.

### 736 **Declarations of interest**

737 All authors declare no conflict of interests.

### 738 **Acknowledgements and funding sources**

739 MP is funded by the EPSRC and MRC Centre for Doctoral Training in Next Generation Statistical  
740 Science: The Oxford-Warwick Statistics Programme (EP/L016710/1). TEN is supported by the  
741 Wellcome Trust, 100309/Z/12/Z. We would like to thank David Firth, Xavier Didelot, Ioannis Kos-  
742 midis and the anonymous reviewers for their insightful comments about the work. We also thank  
743 Paul Thompson and Xue Hua for the TBM data. Data collection and sharing for this project was

744 funded by the Alzheimer’s Disease Neuroimaging Initiative (ADNI) (National Institutes of Health  
745 Grant U01 AG024904) and DOD ADNI (Department of Defense award number W81XWH-12-2-  
746 0012). ADNI is funded by the National Institute on Aging, the National Institute of Biomed-  
747 ical Imaging and Bioengineering, and through generous contributions from the following: AbbVie,  
748 Alzheimer’s Association; Alzheimer’s Drug Discovery Foundation; Araclon Biotech; BioClinica, Inc.;  
749 Biogen; Bristol-Myers Squibb Company; CereSpir, Inc.; Cogstate; Eisai Inc.; Elan Pharmaceuticals,  
750 Inc.; Eli Lilly and Company; EuroImmun; F. Hoffmann-La Roche Ltd and its affiliated company  
751 Genentech, Inc.; Fujirebio; GE Healthcare; IXICO Ltd.; Janssen Alzheimer Immunotherapy Re-  
752 search & Development, LLC.; Johnson & Johnson Pharmaceutical Research & Development LLC.;  
753 Lumosity; Lundbeck; Merck & Co., Inc.; Meso Scale Diagnostics, LLC.; NeuroRx Research; Neu-  
754 rotrack Technologies; Novartis Pharmaceuticals Corporation; Pfizer Inc.; Piramal Imaging; Servier;  
755 Takeda Pharmaceutical Company; and Transition Therapeutics. The Canadian Institutes of Health  
756 Research is providing funds to support ADNI clinical sites in Canada. Private sector contributions  
757 are facilitated by the Foundation for the National Institutes of Health ([www.fnih.org](http://www.fnih.org)). The grantee  
758 organization is the Northern California Institute for Research and Education, and the study is coor-  
759 dinated by the Alzheimer’s Therapeutic Research Institute at the University of Southern California.  
760 ADNI data are disseminated by the Laboratory for Neuro Imaging at the University of Southern  
761 California.

762       **References**

- 763   Apostolova, L. G., Green, A. E., Babakchanian, S., Hwang, K. S., Chou, Y.-Y., Toga, A. W. and  
764   Thompson, P. M. (2012), ‘Hippocampal atrophy and ventricular enlargement in normal aging,  
765   mild cognitive impairment and alzheimer’s disease’, *Alzheimer disease and associated disorders*  
766   **26**(1), 17.
- 767   Ashburner, J., Barnes, G., Chen, C., Daunizeau, J., Flandin, G., Friston, K., Kiebel, S., Kilner, J.,  
768   Litvak, V., Moran, R. et al. (2014), ‘SPM12 manual’, *London: Wellcome Trust* .
- 769   Ashburner, J. and Friston, K. (2004), Morphometry, in R. S. J. Frackowiak, K. J. Friston, C. D.  
770   Frith, R. J. Dolan, C. J. Price, S. Zeki, J. T. Ashburner and W. D. Penny, eds, ‘Human Brain  
771   Function’, 2 edn, Elsevier, chapter 36, pp. 707–722.
- 772   Belloni, A. and Chernozhukov, V. (2011), ‘ $\ell_1$ -penalized quantile regression in high-dimensional  
773   sparse models’, *The Annals of Statistics* **39**(1), 82–130.
- 774   Brockhaus, S., Fuest, A., Mayr, A. and Greven, S. (2018), ‘Signal regression models for location,  
775   scale and shape with an application to stock returns’, *Journal of the Royal Statistical Society:  
776   Series C (Applied Statistics)* **67**(3), 665–686.
- 777   Cabeza, R. and Dennis, N. (2013), Frontal lobes and aging: deterioration and compensation, in  
778   ‘Principles of Frontal Lobe Function’, Vol. 2, Oxford University Press: New York., pp. 628–652.
- 779   Cade, B. S. and Noon, B. R. (2003), ‘A gentle introduction to quantile regression for ecologists’,  
780   *Frontiers in Ecology and the Environment* **1**(8), 412–420.
- 781   Cardot, H., Crambes, C. and Sarda, P. (2005), ‘Quantile regression when the covariates are func-  
782   tions’, *Nonparametric Statistics* **17**(7), 841–856.
- 783   Chen, K. and Müller, H.-G. (2012), ‘Conditional quantile analysis when covariates are functions,  
784   with application to growth data’, *Journal of the Royal Statistical Society: Series B (Statistical  
785   Methodology)* **74**(1), 67–89.  
786   **URL:** <https://rss.onlinelibrary.wiley.com/doi/abs/10.1111/j.1467-9868.2011.01008.x>
- 787   Chen, X., Liu, W., Zhang, Y. et al. (2019), ‘Quantile regression under memory constraint’, *The  
788   Annals of Statistics* **47**(6), 3244–3273.

- 789 Chen, Y., Härdle, W. K., He, Q. and Majer, P. (2018), ‘Risk related brain regions detection and  
790 individual risk classification with 3D image FPCA’, *Statistics & Risk Modeling* **35**(3-4), 89–110.
- 791 Chernozhukov, V., Fernández-Val, I. and Galichon, A. (2010), ‘Quantile and probability curves  
792 without crossing’, *Econometrica* **78**(3), 1093–1125.
- 793 Cole, J. H. (2017), ‘Neuroimaging-derived brain-age: an ageing biomarker?’, *Aging (Albany NY)*  
794 **9**(8), 1861.
- 795 Cole, J. H., Franke, K. and Cherbuin, N. (2019), Quantification of the biological age of the brain  
796 using neuroimaging, in ‘Biomarkers of Human Aging’, Springer, pp. 293–328.
- 797 Cole, J. H., Poudel, R. P., Tsagkrasoulis, D., Caan, M. W., Steves, C., Spector, T. D. and Montana,  
798 G. (2017), ‘Predicting brain age with deep learning from raw imaging data results in a reliable  
799 and heritable biomarker’, *NeuroImage* **163**, 115–124.
- 800 Crainiceanu, C. M., Staicu, A.-M. and Di, C.-Z. (2009), ‘Generalized multilevel functional regres-  
801 sion’, *Journal of the American Statistical Association* **104**(488), 1550–1561.
- 802 Davino, C., Furno, M. and Vistocco, D. (2013), *Quantile regression: theory and applications*, John  
803 Wiley & Sons.
- 804 Delaigle, A. and Hall, P. (2012), ‘Methodology and theory for partial least squares applied to  
805 functional data’, *The Annals of Statistics* **40**(1), 322–352.
- 806 Dennis, N. A. and Cabeza, R. (2011), Neuroimaging of healthy cognitive aging, in ‘The handbook  
807 of aging and cognition’, Psychology Press, pp. 10–63.
- 808 Denver, P. and McClean, P. L. (2018), ‘Distinguishing normal brain aging from the development of  
809 Alzheimer’s disease: inflammation, insulin signaling and cognition’, *Neural regeneration research*  
810 **13**(10), 1719.
- 811 Febrero-Bande, M., Galeano, P. and González-Manteiga, W. (2017), ‘Functional principal compo-  
812 nent regression and functional partial least-squares regression: an overview and a comparative  
813 study’, *International Statistical Review* **85**(1), 61–83.
- 814 Ferraty, F. and Vieu, P. (2006), *Nonparametric functional data analysis: theory and practice*,  
815 Springer Science & Business Media.

- 816 Fitzenberger, B., Koenker, R. and Machado, J. A. (2013), *Economic applications of quantile regres-*  
817 *sion*, Springer Science & Business Media.
- 818 Fjell, A. M., McEvoy, L., Holland, D., Dale, A. M., Walhovd, K. B., Initiative, A. D. N. et al.  
819 (2014), ‘What is normal in normal aging? Effects of aging, amyloid and Alzheimer’s disease on  
820 the cerebral cortex and the hippocampus’, *Progress in Neurobiology* **117**, 20–40.
- 821 Franke, K. and Gaser, C. (2019), ‘Ten years of brainAGE as a neuroimaging biomarker of brain  
822 aging: What insights have we gained?’, *Frontiers in Neurology* **10**, 789.  
823 **URL:** <https://www.frontiersin.org/article/10.3389/fneur.2019.00789>
- 824 Franke, K., Luders, E., May, A., Wilke, M. and Gaser, C. (2012), ‘Brain maturation: predicting  
825 individual BrainAGE in children and adolescents using structural MRI’, *Neuroimage* **63**(3), 1305–  
826 1312.
- 827 Freedman, D. and Diaconis, P. (1981), ‘On the histogram as a density estimator:  $L_2$  theory’,  
828 *Probability theory and related fields* **57**(4), 453–476.
- 829 Friston, K. J., Holmes, A. P., Worsley, K. J., Poline, J.-P., Frith, C. D. and Frackowiak, R. S.  
830 (1994), ‘Statistical parametric maps in functional imaging: a general linear approach’, *Human*  
831 *brain mapping* **2**(4), 189–210.
- 832 Happ, C., Greven, S. and Schmid, V. J. (2018), ‘The impact of model assumptions in scalar-on-  
833 image regression’, *Statistics in medicine* **37**(28), 4298–4317.
- 834 Heinze, G., Wallisch, C. and Dunkler, D. (2018), ‘Variable selection—a review and recommendations  
835 for the practicing statistician’, *Biometrical Journal* **60**(3), 431–449.
- 836 Higham, N. J. (2009), ‘Cholesky factorization’, *Wiley Interdisciplinary Reviews: Computational*  
837 *Statistics* **1**(2), 251–254.
- 838 Horváth, L. and Kokoszka, P. (2012), *Inference for functional data with applications*, Vol. 200,  
839 Springer Science & Business Media.
- 840 Hua, X., Hibar, D. P., Ching, C. R., Boyle, C. P., Rajagopalan, P., Gutman, B. A., Leow, A. D.,  
841 Toga, A. W., Jack Jr, C. R., Harvey, D., Weiner, M. W., Thompson, P. M. and the Alzheimer’s

- 842 Disease Neuroimaging Initiative (2013), ‘Unbiased tensor-based morphometry: improved robust-  
843 ness and sample size estimates for Alzheimer’s disease clinical trials’, *Neuroimage* **66**, 648–661.
- 844 Hua, X., Leow, A. D., Lee, S., Klunder, A. D., Toga, A. W., Lepore, N., Chou, Y.-Y., Brun, C.,  
845 Chiang, M.-C., Barysheva, M. et al. (2008), ‘3D characterization of brain atrophy in Alzheimer’s  
846 disease and mild cognitive impairment using tensor-based morphometry’, *Neuroimage* **41**(1), 19–  
847 34.
- 848 James, G. M., Wang, J. and Zhu, J. (2009), ‘Functional linear regression that’s interpretable’, *The*  
849 *Annals of Statistics* **37**(5A), 2083–2108.
- 850 Kane, M. J., Emerson, J. and Weston, S. (2013), ‘Scalable strategies for computing with massive  
851 data’, *Journal of Statistical Software* **55**(14), 1–19.  
852 **URL:** <http://www.jstatsoft.org/v55/i14/>
- 853 Kato, K. (2012), ‘Estimation in functional linear quantile regression’, *The Annals of Statistics*  
854 **40**(6), 3108–3136.  
855 **URL:** <https://arxiv.org/pdf/1202.4850.pdf>
- 856 Koenker, R. and Bassett, G. (1978), ‘Regression quantiles’, *Econometrica: journal of the Econo-*  
857 *metric Society* pp. 33–50.
- 858 Koenker, R. and Hallock, K. F. (2001), ‘Quantile regression’, *Journal of economic perspectives*  
859 **15**(4), 143–156.
- 860 Kokoszka, P. and Reimherr, M. (2017), *Introduction to functional data analysis*, CRC Press.
- 861 Lockhart, S. N. and DeCarli, C. (2014), ‘Structural imaging measures of brain aging’, *Neuropsy-*  
862 *chology review* **24**(3), 271–289.
- 863 MacPherson, S. and Cox, S. (2017), ‘The frontal ageing hypothesis: Evidence from normal ageing  
864 and dementia.’
- 865 Mayr, A., Hothorn, T. and Fenske, N. (2012), ‘Prediction intervals for future BMI values of in-  
866 dividual children – a non-parametric approach by quantile boosting’, *BMC Medical Research*  
867 *Methodology* **12**(1), 6.

- 868 Meinshausen, N. (2006), ‘Quantile regression forests’, *Journal of Machine Learning Research*  
869 **7**(Jun), 983–999.
- 870 Morris, J. S. (2015), ‘Functional regression’, *Annual Review of Statistics and Its Application* **2**, 321–  
871 359.  
872 **URL:** <https://www.annualreviews.org/doi/pdf/10.1146/annurev-statistics-010814-020413>
- 873 Mosteller, F. and Tukey, J. W. (1977), *Data analysis and regression: a second course in statistics*,  
874 Addison-Wesley Series in Behavioral Science: Quantitative Methods, Pearson.
- 875 Mueller, S. G., Weiner, M. W., Thal, L. J., Petersen, R. C., Jack, C. R., Jagust, W., Trojanowski,  
876 J. Q., Toga, A. W. and Beckett, L. (2005), ‘Ways toward an early diagnosis in Alzheimer’s disease:  
877 the Alzheimer’s Disease Neuroimaging Initiative (ADNI)’, *Alzheimer’s & Dementia* **1**(1), 55–66.
- 878 Müller, H.-G. and Stadtmüller, U. (2005), ‘Generalized functional linear models’, *the Annals of*  
879 *Statistics* **33**(2), 774–805.
- 880 Muschelli, J., Sweeney, E., Lindquist, M. and Crainiceanu, C. (2015), ‘fslr: Connecting the FSL  
881 software with R’, *The R journal* **7**(1), 163.
- 882 Myers, J. L., Well, A. D. and Lorch Jr, R. F. (2013), *Research design and statistical analysis*,  
883 Routledge.
- 884 Penny, W. D., Friston, K. J., Ashburner, J. T., Kiebel, S. J. and Nichols, T. E. (2011), *Statistical*  
885 *parametric mapping: the analysis of functional brain images*, Elsevier.
- 886 Preul, C., Hund-Georgiadis, M., Forstmann, B. U. and Lohmann, G. (2006), ‘Characterization  
887 of cortical thickness and ventricular width in normal aging: a morphometric study at 3 tesla’,  
888 *Journal of Magnetic Resonance Imaging: An Official Journal of the International Society for*  
889 *Magnetic Resonance in Medicine* **24**(3), 513–519.
- 890 Privé, F., Aschard, H., Ziyatdinov, A. and Blum, M. G. (2018), ‘Efficient analysis of large-scale  
891 genome-wide data with two r packages: bigstatsr and bigsnpr’, *Bioinformatics* .  
892 **URL:** <https://doi.org/10.1093/bioinformatics/bty185>
- 893 Ramsay, J. O. and Silverman, B. W. (2005), *Functional Data Analysis*, Springer Series in Statistics,  
894 Springer.



- 895 Reiss, P. T., Goldsmith, J., Shang, H. L. and Ogden, R. T. (2017), ‘Methods for scalar-on-function  
896 regression’, *International Statistical Review* **85**(2), 228–249.  
897 **URL:** <https://onlinelibrary.wiley.com/doi/epdf/10.1111/insr.12163>
- 898 Reiss, P. T. and Ogden, R. T. (2010), ‘Functional generalized linear models with images as predic-  
899 tors’, *Biometrics* **66**(1), 61–69.  
900 **URL:** <https://onlinelibrary.wiley.com/doi/epdf/10.1111/j.1541-0420.2009.01233.x>
- 901 Rigby, R. A. and Stasinopoulos, D. M. (2005), ‘Generalized additive models for location, scale and  
902 shape’, *Journal of the Royal Statistical Society: Series C (Applied Statistics)* **54**(3), 507–554.
- 903 Ruigrok, A. N., Salimi-Khorshidi, G., Lai, M.-C., Baron-Cohen, S., Lombardo, M. V., Tait, R. J. and  
904 Suckling, J. (2014), ‘A meta-analysis of sex differences in human brain structure’, *Neuroscience*  
905 *& Biobehavioral Reviews* **39**, 34–50.
- 906 Scheinost, D., Noble, S., Horien, C., Greene, A. S., Lake, E. M., Salehi, M., Gao, S., Shen, X.,  
907 O’Connor, D., Barron, D. S., Yip, S. W., Rosenberg, M. D. and Constable, R. T. (2019),  
908 ‘Ten simple rules for predictive modeling of individual differences in neuroimaging’, *Neuroim-*  
909 *age* **193**, 35–45.
- 910 Sherwood, B. and Maidman, A. (2017), *rqPen: Penalized Quantile Regression*. R package version  
911 2.0.  
912 **URL:** <https://CRAN.R-project.org/package=rqPen>
- 913 Smith, S. M., Vidaurre, D., Alfaro-Almagro, F., Nichols, T. E. and Miller, K. L. (2019), ‘Estimation  
914 of brain age delta from brain imaging’, *Neuroimage* **200**, 528–539.
- 915 Sone, D., Beheshti, I., Maikusa, N., Ota, M., Kimura, Y., Sato, N., Koepp, M. and Matsuda, H.  
916 (2019), ‘Neuroimaging-based brain-age prediction in diverse forms of epilepsy: a signature of  
917 psychosis and beyond’, *Molecular psychiatry* pp. 1–10.
- 918 Sudlow, C., Gallacher, J., Allen, N., Beral, V., Burton, P., Danesh, J., Downey, P., Elliott, P.,  
919 Green, J., Landray, M., Liu, B., Matthews, P., Ong, G., Pell, J., Silman, A., Young, A., Sprosen,  
920 T., Peakman, T. and Collins, R. (2015), ‘UK Biobank: an open access resource for identifying the  
921 causes of a wide range of complex diseases of middle and old age’, *PLoS medicine* **12**(3), e1001779.

- 922 Tibshirani, R. (1996), ‘Regression shrinkage and selection via the lasso’, *Journal of the Royal*  
923 *Statistical Society: Series B (Methodological)* **58**(1), 267–288.
- 924 Varatharajah, Y., Baradwaj, S., Kiraly, A., Ardila, D., Iyer, R., Shetty, S. and Kohlhoff, K. (2018),  
925 ‘Predicting brain age using structural neuroimaging and deep learning’, *bioRxiv* p. 497925.
- 926 Wang, J., Knol, M. J., Tiulpin, A., Dubost, F., de Bruijne, M., Vernooij, M. W., Adams, H. H. H.,  
927 Ikram, M. A., Niessen, W. J. and Roshchupkin, G. V. (2019), ‘Gray matter age prediction as a  
928 biomarker for risk of dementia’, *Proceedings of the National Academy of Sciences* **116**(42), 21213–  
929 21218.  
930 **URL:** <https://www.pnas.org/content/early/2019/09/30/1902376116>
- 931 Wang, L. (2013), ‘The  $L_1$  penalized LAD estimator for high dimensional linear regression’, *Journal*  
932 *of Multivariate Analysis* **120**, 135–151.
- 933 Yankner, B. A., Lu, T. and Loerch, P. (2008), ‘The aging brain’, *Annu. Rev. pathmechdis. Mech.*  
934 *Dis.* **3**, 41–66.
- 935 Yao, F., Sue-Chee, S. and Wang, F. (2017), ‘Regularized partially functional quantile regression’,  
936 *Journal of Multivariate Analysis* **156**, 39–56.  
937 **URL:** <https://www.sciencedirect.com/science/article/pii/S0047259X17300684>
- 938 Yoo, K., Rosenberg, M. D., Hsu, W.-T., Zhang, S., Li, C.-S. R., Scheinost, D., Constable, R. T. and  
939 Chun, M. M. (2018), ‘Connectome-based predictive modeling of attention: Comparing different  
940 functional connectivity features and prediction methods across datasets’, *Neuroimage* **167**, 11–22.
- 941 Zhou, K. Q. and Portnoy, S. L. (1996), ‘Direct use of regression quantiles to construct confidence  
942 sets in linear models’, *The Annals of Statistics* **24**(1), 287–306.
- 943 Zhou, Y., Zhao, L., Zhou, N., Zhao, Y., Marino, S., Wang, T., Sun, H., Toga, A. and Dinov, I.  
944 (2019), ‘Predictive big data analytics using the UK Biobank data’, *Scientific Reports* **9**(1), 6012.